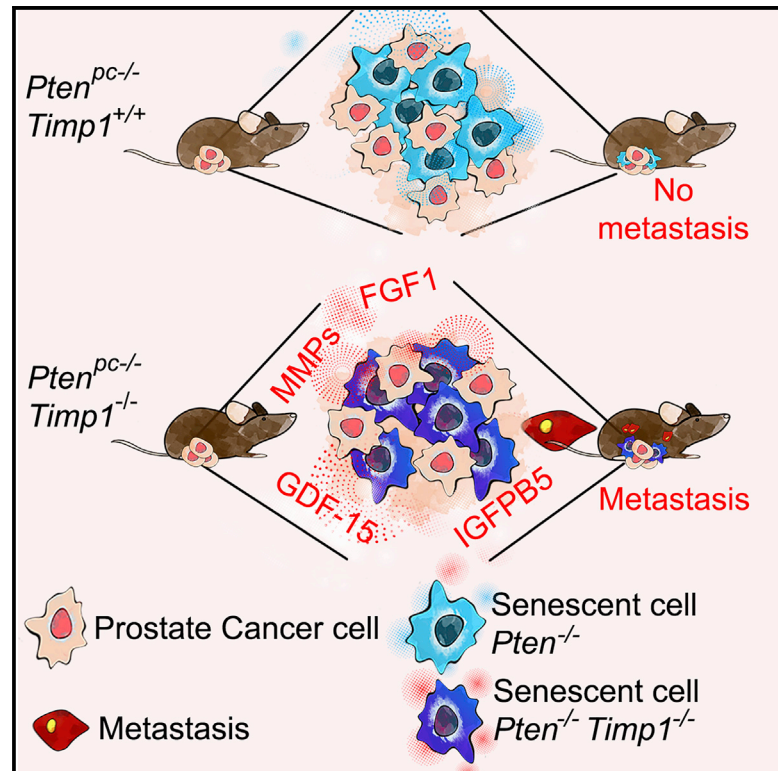


Senescence Reprogramming by TIMP1 Deficiency Promotes Prostate Cancer Metastasis

Graphical Abstract



Authors

Ilaria Guccini, Ajinkya Revandkar, Mariantonietta D'Ambrosio, ..., Peter Wild, Gerda Egger, Andrea Alimonti

Correspondence

andrea.alimonti@ior.usi.ch

In Brief

Guccini et al. show that TIMP1 loss switches senescence from a tumor-suppressive to a pro-metastatic process in prostate cancer mouse models. Pharmacological targeting of *TIMP1*-deficient senescent tumor cells impedes metastases in mice, thereby validating the therapeutic potential of senolytic therapy in prostate cancer.

Highlights

- TIMP1 is a gatekeeper that limits senescent tumor cells from promoting metastases
- Pharmacological elimination of senescent tumor cells impairs metastases formation
- *TIMP1* loss reprograms the SASP to promote cell invasion and migration
- *TIMP1* deficiency is frequently associated with PTEN loss and epigenetic silencing

Article

Senescence Reprogramming by TIMP1 Deficiency Promotes Prostate Cancer Metastasis

Ilaria Guccini,^{1,2,19} Ajinkya Revandkar,^{1,16,19} Mariantonietta D'Ambrosio,^{1,3,16} Manuel Colucci,^{1,3,16} Emiliano Pasquini,^{1,16} Simone Mosole,^{1,16} Martina Troiani,^{1,16} Daniela Brina,^{1,16} Raheleh Sheibani-Tezerji,⁴ Angela Rita Elia,^{1,16} Andrea Rinaldi,^{1,16} Nicolò Pernigoni,^{1,16} Jan Hendrik Rüschoff,⁵ Susanne Dettwiler,⁵ Angelo M. De Marzo,⁶ Emmanuel S. Antonarakis,⁷ Costanza Borrelli,⁸ Andreas E. Moor,⁸ Ramon Garcia-Escudero,^{9,10,11} Abdullah Alajati,^{1,16} Giuseppe Attanasio,^{1,16} Marco Losa,¹² Holger Moch,⁵ Peter Wild,^{13,14} Gerda Egger,^{4,15} and Andrea Alimonti^{1,16,17,18,20,*}

¹Institute of Oncology Research (IOR), Oncology Institute of Southern Switzerland (IOSI), Bellinzona 6500, Switzerland

²Institute of Molecular Health Sciences, ETH Zurich, Zurich 8093, Switzerland

³Faculty of Biology and Medicine, University of Lausanne UNIL, Lausanne 1011, Switzerland

⁴Ludwig Boltzmann Institute Applied Diagnostics, 1090 Vienna, Austria

⁵Department of Pathology and Molecular Pathology, University Hospital Zurich (USZ), Zurich 8091, Switzerland

⁶Departments of Pathology, Urology and Oncology, Sidney Kimmel Comprehensive Cancer Center, The Johns Hopkins University School of Medicine, Baltimore, MD 21231, USA

⁷Departments of Oncology and Urology, Sidney Kimmel Comprehensive Cancer Center, The Johns Hopkins University School of Medicine, Baltimore, MD 21287, USA

⁸Department of Biosystems Science and Engineering, ETH Zurich, Basel 4058, Switzerland

⁹Molecular Oncology Unit, CIEMAT, Madrid 28040, Spain

¹⁰Biomedicine Research Institute, Hospital 12 Octubre, Madrid 28041, Spain

¹¹CIBERONC, Madrid 28029, Spain

¹²Anatomical Pathology Specialization Unit, Toma Advanced Biomedical Assay, Busto Arsizio 21052, Italy

¹³Dr. Senckenberg Institute of Pathology, University Hospital Frankfurt, 60596 Frankfurt Am Main, Germany

¹⁴Frankfurt Institute for Advanced Studies (FIAS), Frankfurt 60438, Germany

¹⁵Department of Pathology, Medical University of Vienna, 1090 Vienna, Austria

¹⁶Università della Svizzera Italiana, Lugano 6900, Switzerland

¹⁷Department of Medicine, University of Padua, Padua 35128, Italy

¹⁸Department of Health Sciences and Technology (D-HEST) ETH Zurich, Zurich 8093, Switzerland

¹⁹These authors contributed equally

²⁰Lead Contact

*Correspondence: andrea.alimonti@ior.usi.ch

<https://doi.org/10.1016/j.ccell.2020.10.012>

SUMMARY

Metastases account for most cancer-related deaths, yet the mechanisms underlying metastatic spread remain poorly understood. Recent evidence demonstrates that senescent cells, while initially restricting tumorigenesis, can induce tumor progression. Here, we identify the metalloproteinase inhibitor *TIMP1* as a molecular switch that determines the effects of senescence in prostate cancer. Senescence driven either by *PTEN* deficiency or chemotherapy limits the progression of prostate cancer in mice. *TIMP1* deletion allows senescence to promote metastasis, and elimination of senescent cells with a senolytic BCL-2 inhibitor impairs metastasis. Mechanistically, *TIMP1* loss reprograms the senescence-associated secretory phenotype (SASP) of senescent tumor cells through activation of matrix metalloproteinases (MMPs). Loss of *PTEN* and *TIMP1* in prostate cancer is frequent and correlates with resistance to docetaxel and worst clinical outcomes in patients treated in an adjuvant setting. Altogether, these findings provide insights into the dual roles of tumor-associated senescence and can potentially impact the treatment of prostate cancer.

INTRODUCTION

Metastatic prostate cancer is one of the leading causes of cancer-related deaths in men worldwide (Rawla, 2019). While patients with localized and advanced prostate tumors are sensitive to androgen-deprivation therapies (ADT) and are highly curable, metastatic prostate cancer patients acquire resistance to ADT

and succumb to this disease (Litwin and Tan, 2017). Thus, understanding the molecular events that drive the transition from localized to metastatic prostate cancer would help to develop more effective therapies for prostate cancer patients. Senescence is a stable cell-cycle arrest that occurs in both primary and cancer cells in response to oncogene overexpression, DNA damage accumulation, metabolic stresses, and anti-cancer therapies

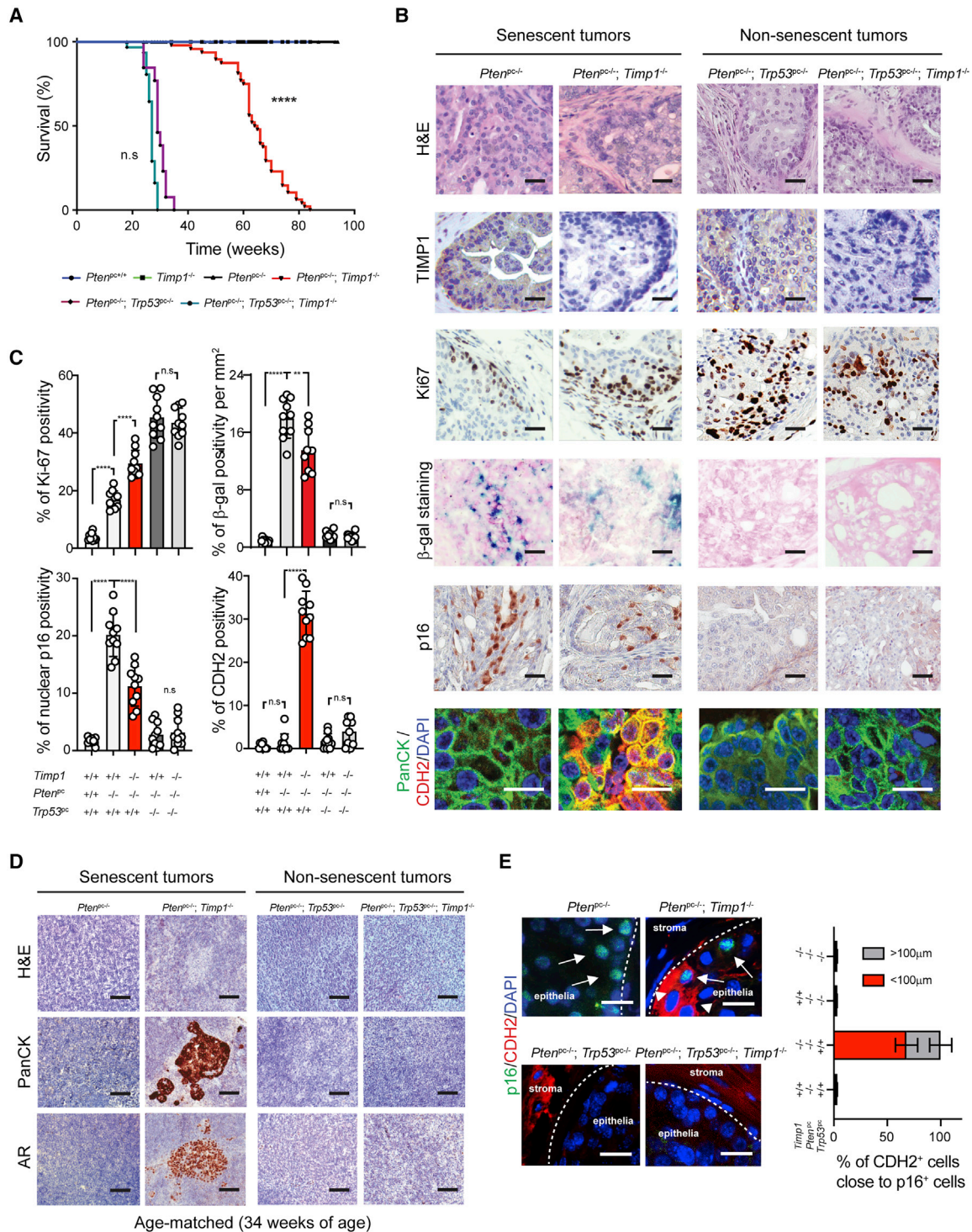


Figure 1. *Pten/Timp1*-Null Tumors Displayed Tumor Progression and Metastases with Decreased Lifespan in Mice

(A) Percentage survival of $Pten^{pc+/+}$, $Timp1^{-/-}$, $Pten^{pc-/-}$, $Pten^{pc-/-}; Timp1^{-/-}$, $Pten^{pc-/-}; Trp53^{pc-/-}$, and $Pten^{pc-/-}; Trp53^{pc-/-}; Timp1^{-/-}$ mice in weeks. Kaplan-Meier survival curves were compared by Mantel-Cox log rank test; $n = 210$ in total.

(B) Representative IHC images of H&E, TIMP1, Ki67, SA- β -gal, and p16 of senescent $Pten^{pc-/-}$ and $Pten^{pc-/-}; Timp1^{-/-}$ tumors versus non-senescent $Pten^{pc-/-}; Trp53^{pc-/-}$ and $Pten^{pc-/-}; Trp53^{pc-/-}; Timp1^{-/-}$ tumors (40 \times). Scale bars, 50 μm . Immunofluorescence (IF) staining images show the expression of pan-cytokeratin (PanCK), CDH2, and DAPI in all four tumor sections, magnification 400 \times . Scale bars, 50 μm . $n = 10$ for each genotype.

(C) Percentage of Ki67, β -gal positivity per mm^2 , nuclear p16 determined by IHC staining, and CDH2 positivity determined by double-positive PanCK and CDH2 cells by IF in $Pten^{pc+/+}$, $Pten^{pc-/-}$, $Pten^{pc-/-}; Timp1^{-/-}$, $Pten^{pc-/-}; Trp53^{pc-/-}$, and $Pten^{pc-/-}; Trp53^{pc-/-}; Timp1^{-/-}$ prostate tissue/tumor samples, $n = 10$ for each genotype.

(legend continued on next page)

(Gorgoulis et al., 2019; Sieben et al., 2018). The contribution of senescence to cancer development has been somewhat controversial and highly complex. Several findings in genetically engineered mouse models (GEMMs) demonstrate that senescence works as a fail-safe response that opposes tumor progression by promoting tumor cell growth arrest and an anti-tumor immune response (Chen et al., 2005; Collado et al., 2005; Kasthuber and Lowe, 2017; Xue et al., 2007). However, recent evidence demonstrates that therapy-induced senescence (TIS) can promote metastases (Camphausen et al., 2001; Demaria et al., 2017; Kim et al., 2017). These contradicting results can be explained by the senescence-associated secretory phenotype (SASP) of tumor cells. Senescent cells secrete a variety of pro-inflammatory factors in the tumor microenvironment that can support the survival, outgrowth, and migration of tumor cells (Demaria et al., 2017; Faget et al., 2019; Laberge et al., 2012; Lecot et al., 2016). Thus, whether the type or the trigger of senescence accounts for its tumor-promoting or tumor-suppressive function remains elusive. Identifying those tumors where senescence would promote tumor growth and metastases instead of tumor suppression will help to (1) stratify patients where senescence-inducing therapies should be administered with caution and (2) select patients to be treated with compounds that eliminate senescent cells (senolytic therapies) or inhibit the deleterious effect of the SASPs.

Pten-null prostate conditional mice (hereafter termed *Pten*^{pc-/-}) develop indolent prostate tumors characterized by a robust p53-dependent senescence response that opposes tumor progression without driving metastases (Chen et al., 2005). Intriguingly, further enhancement of senescence in *Pten*^{pc-/-} tumors by docetaxel treatment does not trigger metastases (Di Mitri et al., 2014; Toso et al., 2014). We, therefore, put forward the hypothesis that the secretome of *Pten*-loss induced cellular senescence could either lack factors that support tumor progression or contain “metastases inhibitory” factors. Here, we report that *TIMP1*-loss by reprogramming the SASP, switches the tumor-suppressive response induced by *PTEN*-loss and TIS into a tumor-promoting and metastatic response. Of note, we demonstrate that senolytic therapies can efficiently prevent the spreading of metastases in senescent tumors lacking *TIMP1*.

RESULTS

Timp1-Loss in Senescent *Pten*-Null Tumors Promoted Tumor Progression and Metastases *In Vivo*

To characterize the secretome of *Pten*-null tumors, we performed gene expression profiling of cytokines and cytokine-related factors in *Pten*^{pc-/-} senescent and in *Pten*^{pc-/-}; *Trp53*^{pc-/-} non-senescent tumors. While we confirmed the presence of cytokines, which were specifically up- and down-

regulated in *Pten*^{pc-/-} senescent tumors (“core-SASP”) (Coppe et al., 2010a; Coppe et al., 2010b), we also found a number of upregulated secreted factors that were “senescence-unrelated” since they were present in both *Pten*^{pc-/-} and *Pten*^{pc-/-}; *Trp53*^{pc-/-} tumors (Figure S1A). Gene expression profile analysis of senescence-unrelated factors revealed that tissue inhibitor of metalloproteinases 1 (*Timp1*) was the most upregulated factor (Figure S1A; Tables S1 and S2). *TIMP1* is a pan-matrix metalloproteinases (Pan-MMPs) inhibitor, in particular of MMP2 and MMP9, and a regulator of cell invasion and migration in cancer. *TIMP1* is part of a family of three additional MMP inhibitory factors *TIMP2*, *TIMP3*, and *TIMP4* (Jackson et al., 2017). Of note, *Timp1* was not only upregulated at RNA but also at protein levels (Figures S1A–S1C). Interestingly, while the levels of *Timp1* increased in *Pten*-deficient tumors, the levels of the other *Timps* did not change when compared with normal prostates (Figure S1C). Given the high levels of *TIMP1* in *Pten*^{pc-/-} prostate tumors, we hypothesized that *TIMP1* could prevent senescence from triggering metastases in *Pten*^{pc-/-} senescent tumors and could act as a metastases inhibitory factor.

Thus, we generated *Timp1* deletion in both the *Pten*^{pc-/-} and *Pten*^{pc-/-}; *Trp53*^{pc-/-} mice (hereafter termed *Pten*^{pc-/-}; *Timp1*^{-/-} and *Pten*^{pc-/-}; *Trp53*^{pc-/-}; *Timp1*^{-/-}). Strikingly, loss of *Timp1* affected the survival of *Pten*^{pc-/-} but not of *Pten*^{pc-/-}; *Trp53*^{pc-/-} mice (Figure 1A). Genetic inactivation of *Timp1* was confirmed by immunohistochemistry (IHC) and real-time PCR, while gelatin-zymography assay showed increased activity of MMP2 and MMP9, in both *Pten*^{pc-/-}; *Timp1*^{-/-} and *Pten*^{pc-/-}; *Trp53*^{pc-/-}; *Timp1*^{-/-} tumors (Figures 1B and S1C–S1E). Similar to *Pten*^{pc-/-}; *Pten*^{pc-/-}; *Timp1*^{-/-} mice developed focally invasive prostate cancer by age 12 weeks (Figures 1B and S1F). In contrast, age-matched *Pten*^{pc-/-}; *Trp53*^{pc-/-} and *Pten*^{pc-/-}; *Trp53*^{pc-/-}; *Timp1*^{-/-} mice develop highly aggressive and invasive prostate cancer and die earlier due to bladder obstruction and renal failure (Chen et al., 2005). Finally, *Timp1*^{-/-} mice showed no prostate neoplasia beyond 2 years of age (Figure S1F). Histopathological analysis and Ki67 staining in age-matched mice of different genotypes showed an increased aggressiveness and proliferation of *Pten*^{pc-/-}; *Timp1*^{-/-} tumors compared with *Pten*^{pc-/-} (Figures 1B, 1C, and S1F). However, *Pten*^{pc-/-}; *Timp1*^{-/-} tumors retained the senescence response caused by loss of *Pten* as detected by quantification of senescence-associated β -galactosidase (SA- β -gal) and nuclear p16 positivity (Figures 1B and 1C). Surprisingly, age-matched analysis (17–25 and 26–34 weeks) in mice of different genotypes showed that only *Pten*^{pc-/-}; *Timp1*^{-/-} mice developed lumbar lymph node (LN) metastases despite the finding that these mice had smaller primary tumors than *Pten*^{pc-/-}; *Trp53*^{pc-/-} and *Pten*^{pc-/-}; *Trp53*^{pc-/-}; *Timp1*^{-/-} mice (Figures 1D, S2A, and S2B). Metastatic dissemination was observed as deposition of pan-cytokeratin- and androgen receptor-positive

(D) Representative images of H&E, PanCK, and androgen receptor (AR) staining in lymph nodes (LN) metastasis from age-matched *Pten*^{pc-/-} (n = 11), *Pten*^{pc-/-}; *Timp1*^{-/-} (n = 12), *Pten*^{pc-/-}; *Trp53*^{pc-/-} (n = 13), and *Pten*^{pc-/-}; *Trp53*^{pc-/-}; *Timp1*^{-/-} (n = 13) mice.

(E) IF staining and quantification for CDH2, p16, and DAPI in *Pten*^{pc-/-}, *Pten*^{pc-/-}; *Timp1*^{-/-}, *Pten*^{pc-/-}; *Trp53*^{pc-/-}, and *Pten*^{pc-/-}; *Trp53*^{pc-/-}; *Timp1*^{-/-} prostate tumors. Arrows indicate senescent nuclear p16-stained cells, whereas arrowheads indicate the CDH2-positive cells found in close proximity (400 \times), n = 12. Bar graph represents the distance of senescent cells and metastatic cells. Scale bars, 50 μ m.

The p values in (C) were determined by Student’s t test (unpaired two-tailed), n.s., not significant; **p < 0.01, ****p < 0.0001. Data are represented as mean \pm SEM. See also Figures S1 and S2 and Tables S1 and S2.

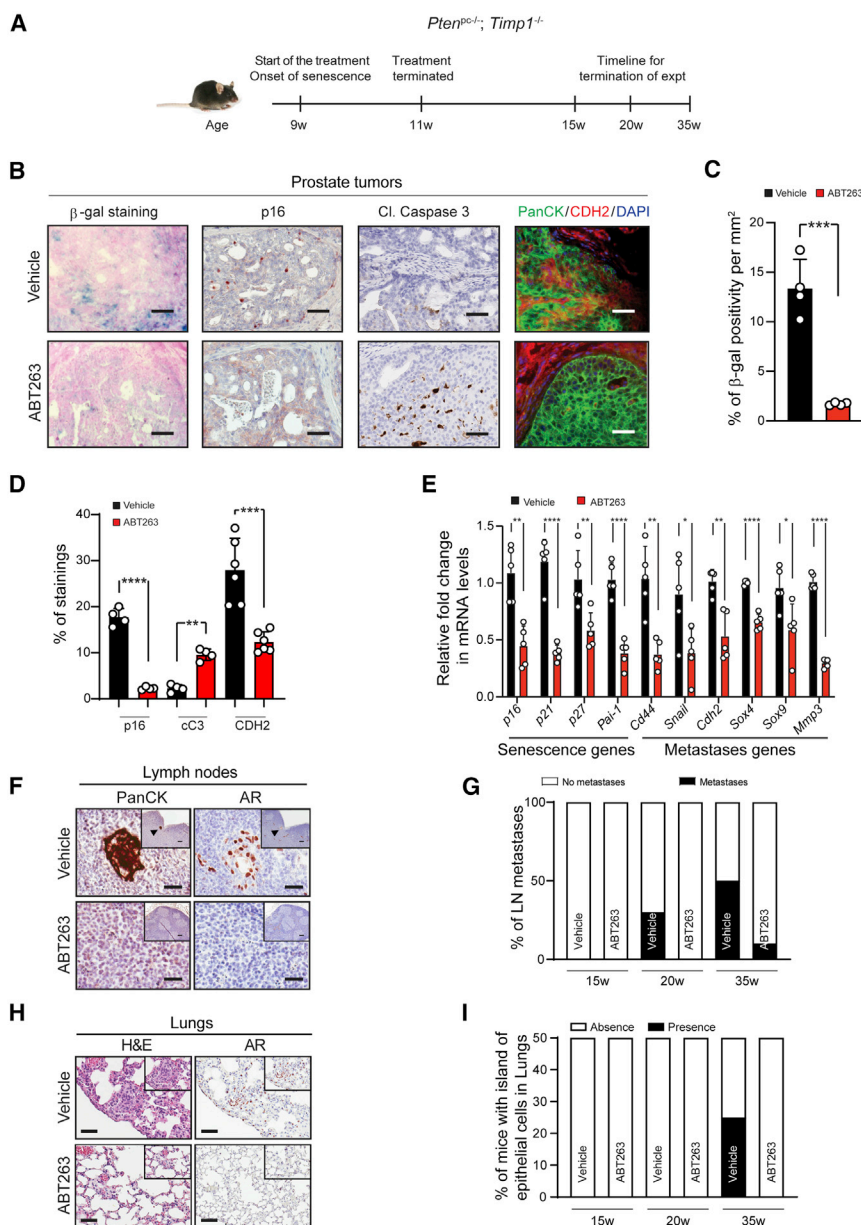


Figure 2. Selective Elimination of Senescent Cells from *Pten/Timp1*-Null Tumors by ABT263-Impaired Metastases

(A) Timeline for ABT263 treatment in *Pten*^{pc-/-}; *Timp1*^{-/-} mice.

(B) Representative images of SA- β -gal, p16, and cleaved caspase-3 (cC3) staining of anterior prostate (AP) tumor sections of mice treated with vehicle and ABT263 at 15 weeks (w). IF staining for PanCK, CDH2, and DAPI in *Pten*^{pc-/-}; *Timp1*^{-/-} tumors upon treatment with ABT263 (20w).

(C) Percentage of β -gal positivity per mm² in *Pten*^{pc-/-}; *Timp1*^{-/-} tumors treated with vehicle and ABT263 as represented in (B), n = 4.

(D) Percentage of p16, cC3, and CDH2 positivity in *Pten*^{pc-/-}; *Timp1*^{-/-} tumors treated with vehicle and ABT263 as represented in (B), n = 4 and 6.

(E) Relative fold change in mRNA levels of senescence- and metastases-related genes in *Pten*^{pc-/-}; *Timp1*^{-/-} tumors treated with vehicle and ABT263, n = 5.

(F) Representative IHC images of PanCK and AR stainings in LNs from *Pten*^{pc-/-}; *Timp1*^{-/-} mice treated with vehicle and ABT263. Insets represent 10 \times magnification of the image shown at 40 \times .

(G) Percentage of LN metastasis from *Pten*^{pc-/-}; *Timp1*^{-/-} mice treated with vehicle and ABT263 as represented in (F), n = 4.

(H) Representative images of H&E and AR tumor epithelial cell deposits as “islands” in lungs of *Pten*^{pc-/-}; *Timp1*^{-/-} mice treated with vehicle and ABT263. Insets represent zoom-in (80 \times) to the region of epithelial cells deposits.

(I) Percentage of mice tumor epithelial cell deposits in lungs at age 35w, n = 8.

All images were taken at 40 \times magnification, unless mentioned otherwise. Scale bars, 50 μ m. The p values were determined by Student’s t test (unpaired two-tailed); *p < 0.05, **p < 0.01, ***p < 0.001, ****p < 0.0001. Data are represented as mean \pm SEM. See also Figure S3.

(Fridlender et al., 2012; Kuroda et al., 2019; Wang et al., 2019; Wynn and Barron, 2010).

Thus, to evaluate the contribution of the tumor immune response in driving this metastatic phenotype we performed a reconstitution experiment with bone marrow (BM) from *Timp1*^{+/+} mice in *Pten*^{pc-/-}; *Timp1*^{-/-} mice (Figure S2H). Fluorescence-activated cell sorting analysis confirmed CD45.1 *Timp1*^{+/+} BM cells in CD45.2 *Pten*^{pc-/-}; *Timp1*^{-/-} mice (Figure S2I). Of note, *Pten*^{pc-/-}; *Timp1*^{-/-}; BM *Timp1*^{+/+} mice showed similar survival and metastatic outcome than *Pten*^{pc-/-}; *Timp1*^{-/-} mice (Figures S2J–S2L). Together, these data demonstrate that the inactivation of TIMP1 in tumor-infiltrating immune cells is not the cause of metastases in this genetic background.

Elimination of Senescent Cells from *Pten/Timp1*-Null Mice Impaired Metastases Formation

Led by the notion that senescence in primary tumors could be responsible for the metastases formation in the *Pten*^{pc-/-}; *Timp1*^{-/-} mice, we treated these mice with navitoclax

prostate tumor cells (Figures 1D and S2A) along with small islands of tumor cells in the lungs (Figures S2C–S2E). Gene expression profile analysis in primary tumors revealed an upregulation of metastases-related genes exclusively in *Pten*^{pc-/-}; *Timp1*^{-/-} tumors (Figure S2F). CDH2 (N-cadherin), SOX4, and SOX9, markers of tumor cell invasion and metastases, were highly expressed in these tumors (Grimm et al., 2019; Suyama et al., 2002; Tanaka et al., 2010). Immunofluorescence (IF) staining and single-molecule fluorescent *in situ* hybridization (smFISH) confirmed these findings and showed that, in *Pten*^{pc-/-}; *Timp1*^{-/-} tumors, senescent cells appeared in the proximity of cells expressing Sox4, Sox9, and Cdh2 (Figures 1B–1E and S2G). In summary, these results indicate that *Timp1*-genetic inactivation in senescent tumors but not in non-senescent tumors results in metastases. TIMP1 is strongly expressed in immune cells in particular in cells of myeloid lineage

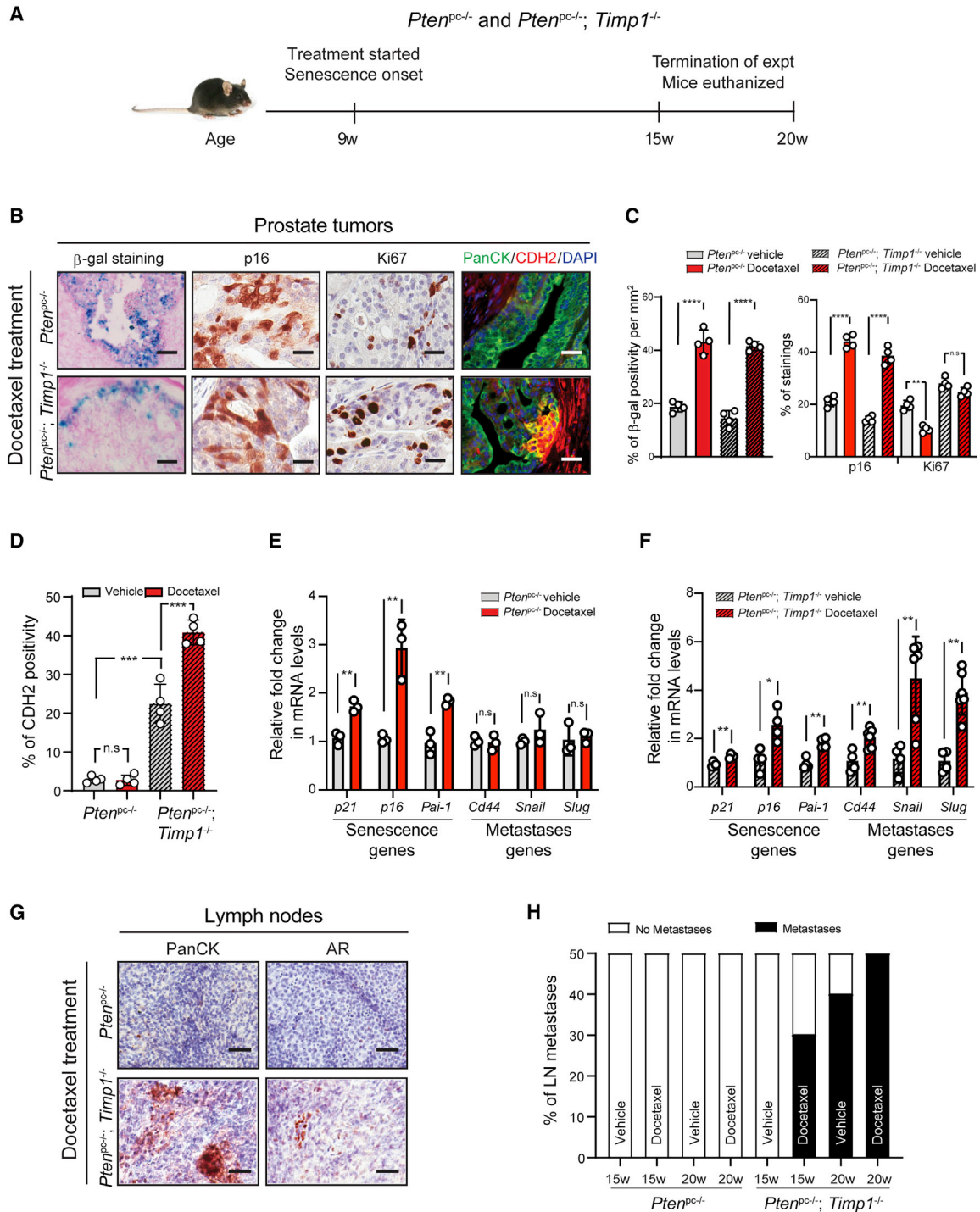


Figure 3. Docetaxel-Enhanced Senescence Accelerated Metastases Formation Only in *Pten/Timp1*-Null Mice

(A) Timeline for docetaxel treatment in *Pten^{pc-/-}* and *Pten^{pc-/-}; Timp1^{-/-}* mice.

(B) Representative IHC images of SA- β -gal, p16, and Ki67 staining and IF of PanCK, CDH2, and DAPI staining of AP tumors from *Pten^{pc-/-}* and *Pten^{pc-/-}; Timp1^{-/-}* mice treated with docetaxel.

(C) Percentage of β -gal, p16, and Ki67 positivity per mm² in vehicle- and docetaxel-treated *Pten^{pc-/-}* and *Pten^{pc-/-}; Timp1^{-/-}* mice, n = 4.

(D) Percentage of PanCK and CDH2 double-positive cells by IF in tumors from vehicle- and docetaxel-treated *Pten^{pc-/-}* and *Pten^{pc-/-}; Timp1^{-/-}* mice, n = 4.

(E) Relative fold change in mRNA levels of senescence- and metastases-related genes in vehicle- and docetaxel-treated *Pten^{pc-/-}* tumors, n = 3.

(F) Relative fold change in mRNA levels of senescence- and metastases-related genes in vehicle- and docetaxel-treated *Pten^{pc-/-}; Timp1^{-/-}* tumors, n = 4 and 6.

(legend continued on next page)

(ABT263), a potent Bcl-2 inhibitor. Senescent tumor cells upregulate *Bcl-2* for survival and hence remain more sensitive to Bcl-2 inhibitors (Calcinotto et al., 2019; Chang et al., 2016; Demaria et al., 2017). In line with these findings, single-cell sequencing analysis in both *Pten*^{pc-/-} and *Pten*^{pc-/-}; *Timp1*^{-/-} tumors showed that senescent tumor cells (expressing *p16Ink4a*, *p19Arf*, *p21Cip1*, *p27kip1*, and *Pai-1*) exclusively expressed high levels of *Bcl2* and displayed a positive correlation (Figures S3A–S3E). Therefore, we treated two cohorts of *Pten*^{pc-/-}; *Timp1*^{-/-} mice with vehicle and ABT263 for 2 weeks. The treatment started at the onset of senescence and ended before the onset of metastases (9–11 weeks old). Mice were sacrificed at different ages in a time course experiment (Figure 2A). IHC analysis for SA- β -gal and p16 confirmed the depletion of senescent cells and an increase in cell death as measured by cleaved caspase-3 staining in the tumors of mice treated with ABT263 (Figures 2B–2D). Strikingly, the elimination of senescent cells by ABT263 also decreased CDH2 staining (Figures 2B and 2D) and the signature of senescence- and metastases-related genes in treated tumors (Figure 2E). In line with these findings, while vehicle mice developed metastases to the LNs and lungs, ABT263-treated mice did not (Figures 2F–2I). These results support the notion that senescent tumor cells trigger metastases and that pharmacological elimination of these cells using ABT263 can efficiently prevent metastatic colonization.

TIS Accelerated Metastases Formation in *Pten/Timp1*-Null Mice

We next determined whether TIS would enhance metastases formation in *Pten*^{pc-/-}; *Timp1*^{-/-} tumors. Hence, we treated a cohort of both *Pten*^{pc-/-} and *Pten*^{pc-/-}; *Timp1*^{-/-} mice with docetaxel, a standard chemotherapy used for the treatment of prostate cancer, known to induce senescence in prostate tumor cells (Di Mitri et al., 2014; Toso et al., 2014). Treatment started at the onset of senescence and terminated before the onset of metastases in both genotypes (Figure 3A). Docetaxel treatment strongly enhanced senescence in both *Pten*^{pc-/-} and *Pten*^{pc-/-}; *Timp1*^{-/-} tumors as determined by SA- β -gal and p16 staining (Figures 3B, 3C, and S4A). However, while *Pten*^{pc-/-} tumors showed a marked decrease in tumor cell proliferation, *Pten*^{pc-/-}; *Timp1*^{-/-} tumors showed no significant difference in proliferation (Figures 3B, 3C, and S4A). Strikingly, TIS resulted in an increased expression of senescence-related genes in both *Pten*^{pc-/-} and *Pten*^{pc-/-}; *Timp1*^{-/-} tumors but enhanced the expression of CDH2 and metastases-related genes selectively in the *Pten*^{pc-/-}; *Timp1*^{-/-} tumors (Figures 3B, 3D, 3F, and S4A). Furthermore, *Pten*^{pc-/-}; *Timp1*^{-/-} mice showed an earlier onset and an increased percentage of metastases upon treatment with docetaxel (Figures 3G and H). In contrast, *Pten*^{pc-/-} mice showed no signs of metastases in both vehicle- and docetaxel-treated mice (Figures 3G and H). Together, these data demonstrate that TIS can promote divergent outcomes in mice with tumors of different genetic backgrounds.

TIS in PTEN/TIMP1-Deficient Human Prostate Cancer Cells Promoted Rapid Metastases Formation *In Vivo*

To further validate these data in a human-relevant setting, we turned to an experimental metastases model wherein we assessed organ colonization ability of human prostate tumor cells in NSG mice. PC3 cells express high levels of TIMP1 and carry homozygous *PTEN* deletion (Gong et al., 2015). We infected these cells with firefly luciferase reporter plasmid to monitor their growth *in vivo* by bioluminescence imaging (BLI) and further knocked down *TIMP1* using shRNA (Figure 4A). Both shCtrl and sh*TIMP1* PC3 cells were intravenously (i.v.) injected in mice. Four weeks after i.v. injections and engraftment of cells, mice were treated with either vehicle or docetaxel for a total of 6 weeks (Figure 4B). Docetaxel treatment enhanced the capability of PC3-sh*TIMP1* cells to colonize the lungs and kidneys (Figures 4C and D). IHC and gene expression profile analysis of kidneys and lungs tumor lesions in the mice treated with docetaxel showed increased expression of markers of senescence (Figures S4B and S4C). Moreover, the average size of the lungs and kidneys tumor lesions in docetaxel-treated sh*TIMP1* mice was significantly bigger than the one of docetaxel-treated shCtrl mice (Figures 4E–4J). Next, we assessed whether the elimination of senescent cells by means of ABT263 could affect the capability of human prostate cancer cells to colonize distant organs *in vivo* (Figure 4K). Strikingly, ABT263 treatment abolished *TIMP1*-deficient tumor cells colonization in docetaxel-treated mice as assessed by BLI and percentage of the lungs and kidneys metastases (Figures 4L–4O). Histopathological analysis further confirmed that ABT263 abrogated tumor cells colonization only in docetaxel-treated mice (Figures 4N–4R). In sum, these results validate the findings from the transgenic mouse model, demonstrating that TIS leads to tumor regression in *TIMP1*-proficient tumors, whereas it accelerates metastases formation in *TIMP1*-deficient prostate cancers, which can be inhibited by subsequent senolytic treatment. These data point at the genetic background of the tumors as a crucial determinant for the distinct outcome of senescence in prostate cancer (CaP).

Timp1-Loss Reprogrammed the SASP of *Pten*-Null Cells and Human Prostate Cancer Cells Treated with Chemotherapy

Next, we sought to determine the mechanism by which senescence contributes to the acquisition of this aggressive tumor future. We took advantage of mouse embryonic fibroblasts and performed proliferation, senescence, cell invasion, and migration assays in *Pten*^{+/+}, *Pten*^{-/-}, *Timp1*^{-/-}, *Pten*^{-/-}; *Timp1*^{-/-}, *Pten*^{-/-}; *Trp53*^{-/-}, and *Pten*^{-/-}; *Trp53*^{-/-}; *Timp1*^{-/-} cells. In line with the *in vivo* evidence, both *Pten*^{-/-} and *Pten*^{-/-}; *Timp1*^{-/-} cells retained a senescence response (Figures 5A and 5B). However, *Pten*^{-/-}; *Timp1*^{-/-} cells had an increased invasive and migratory capability when compared with *Pten*^{-/-} cells or cells of other genetic backgrounds (Figures 5C).

To assess whether the enhanced migratory and invasive capability of *Pten*^{-/-}; *Timp1*^{-/-} cells was mediated by the secretome

(G) Representative IHC images of PanCK and AR staining in LNs from *Pten*^{pc-/-} and *Pten*^{pc-/-}; *Timp1*^{-/-} mice at 20w.

(H) Percentage of LN metastases from *Pten*^{pc-/-} and *Pten*^{pc-/-}; *Timp1*^{-/-} mice treated with vehicle and docetaxel, n = 4.

All images were taken at 40 \times magnification. Scale bars, 50 μ m. All p values were determined by Student's t test (unpaired two-tailed), n.s., not significant; *p < 0.05, **p < 0.01, ***p < 0.001, ****p < 0.0001. Data are represented as mean \pm SEM. See also Figure S4.

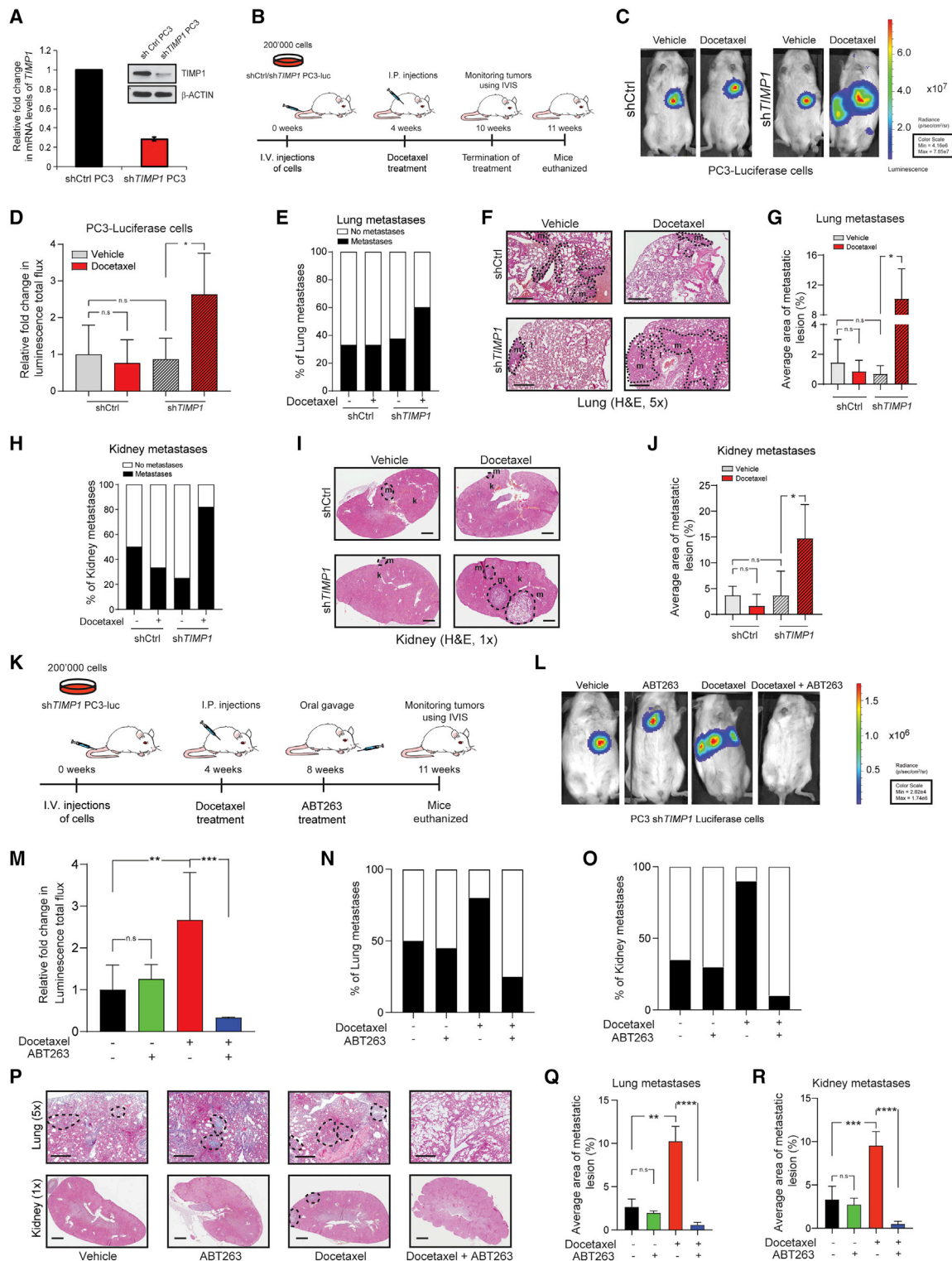


Figure 4. Docetaxel Treatment in *TIMP1*-Deficient Metastatic Human Prostate Tumors Promoted Rapid Colonization to Distal Organs

(A) Validation of *TIMP1* silencing in human PC3 cancer cells by RNA and protein levels. (B) Timeline of the experimental metastases model using PC3 shCtrl and sh*TIMP1* cells expressing luciferase in NSG mice treated with vehicle and docetaxel. (C) Representative bioluminescence imaging (BLI) of mice bearing tumors of respective genotypes treated with vehicle and docetaxel. (D) Bar graph represents relative fold change in bioluminescence signal of total flux in mice with the respective treatments: one-way ANOVA multiple comparison test (Tukey's test), $n = 5$.

(legend continued on next page)

of these cells, we treated $Pten^{-/-}$ and $Pten^{-/-}; Trp53^{-/-}; Timp1^{-/-}$ cells, which lack invasive and migratory potential, with condition media (c.m.) harvested from $Timp1$ -null cells of different genetic backgrounds. Interestingly, we found that only the c.m. from senescent $Pten^{-/-}; Timp1^{-/-}$ cells was capable of triggering cell invasion and migration in $Pten^{-/-}$ and $Pten^{-/-}; Trp53^{-/-}; Timp1^{-/-}$ cells (Figures 5D, S5A, and S5B). These data suggest that $Timp1$ -loss reprograms the secretome of $Pten$ -null cells, and affects the cell invasion and migration in a paracrine manner. Of note, c.m. derived from $Pten^{-/-}; Timp1^{-/-}$ cells pre-treated with either ABT263, Pan-MMPs inhibitor (MMPi) or heat-inactivated was not capable of enhancing cellular invasion and migration in $Pten^{-/-}$ and $Pten^{-/-}; Trp53^{-/-}; Timp1^{-/-}$ cells (Figures 5D and S5A). The effect of ABT263 and Pan-MMPi on senescence and MMP2 activity was assessed by SA- β -gal assay and gelatin-zymography (Figures S5C and S5D). Together, these data demonstrate that $Timp1$ inactivation reprograms the SASP of $Pten$ -null cells by activating the MMPs. MMPs are known to regulate the levels and availability of different secreted factors that can support tumor progression. Activation of MMPs can release secreted factors from either the cells, the cellular matrix or promote the cleavage of their pro-domain to generate bioavailable active forms. MMPs can also degrade secreted factors having a tumor-suppressive function (Klein and Bischoff, 2011; Nagase et al., 2006; Page-McCaw et al., 2007; Rodriguez et al., 2010; Visse and Nagase, 2003). We thus speculated that activation of MMPs by $Timp1$ -loss in $Pten$ -null cells might differentially regulate the level of secreted factors facilitating invasion and metastases (Kessenbrock et al., 2010; Nagase et al., 2006; Page-McCaw et al., 2007; Rodriguez et al., 2010; Visse and Nagase, 2003). To prove this hypothesis, we harvested the c.m. from $Pten^{-/-}$ and $Pten^{-/-}; Timp1^{-/-}$ cells and performed proteome profile analysis. Coagulation factor III/tissue factor (TF), fibroblast growth factor 1 (FGF1), growth/differentiation factor (GDF-15), (IGFBP-5), interleukin-1 α (IL-1 α) (interleukin-1 α), Serpin F1 (PEDF) were the most significantly and differentially regulated factors in $Pten^{-/-}; Timp1^{-/-}$ compared with $Pten^{-/-}$ cells

whereas $Pten^{-/-}; Trp53^{-/-}$ and $Pten^{-/-}; Timp1^{-/-}; Trp53^{-/-}$ lacked these factors (Figures 5E and S5E). While TF, PEDF, FGF1, and GDF-15 were strongly upregulated, IGFBP-5 and IL-1 α were downregulated in the c.m. of $Pten^{-/-}; Timp1^{-/-}$. To determine the potential involvement of these factors in the migratory phenotype, we treated $Pten^{-/-}$ cells, which do not migrate *in vitro*, with recombinant FGF1 (rFGF1), GDF-15 (rGDF-15), TF (rTF), and PEDF (rPEDF). Only rFGF1 and rGDF-15 promoted cell migration in $Pten^{-/-}$ cells whereas rTF and rPEDF did not (Figure 5F). Furthermore, both $Pten^{-/-}$ and $Pten^{-/-}; Timp1^{-/-}$ cells were treated with recombinant IGFBP-5 (rIGFBP-5) and IL-1 α (rIL-1 α). While rIGFBP-5 resulted in decreased cell migration selectively in $Pten^{-/-}; Timp1^{-/-}$ cells, rIL-1 α did not exert any effect on neither $Pten^{-/-}$ nor $Pten^{-/-}; Timp1^{-/-}$ cell migration (Figure 5F). To validate the relevance of GDF-15 and FGF1, we treated both $Pten^{-/-}$ and $Pten^{-/-}; Timp1^{-/-}$ cells with an inhibitor of FGFR (FGFRi) and a neutralizing antibody of GDF-15 (GDF15Nab). Cell migration analysis confirmed that FGFRi and GDF15Nab selectively blocked the migration of $Pten^{-/-}; Timp1^{-/-}$ cells without affecting $Pten^{-/-}$ cell migration (Figure 5F). Thus, these experiments identify GDF-15, FGF1, and IGFBP-5 as senescence relevant targets that promote cell invasion and migration. These data were further validated in a model of TIS using human prostate tumor cells. Docetaxel treatment triggered senescence in both PC3-shTIMP1 and PC3-shCtrl cells to a similar extent (Figures S6A–S6C). Secretome profile analysis in the c.m. of PC3-shTIMP1 cells treated with docetaxel identified increased levels of GDF-15, FGF2 and decreased levels of IL-1 α , IL-1 β , and IGFBPs as the most deregulated factor when compared with control thereby validating our previous findings in mouse cells (Figures S6D and S6E). The c.m. from docetaxel-treated shTIMP1 cells was also capable of increasing cell migration of PC3 cells (Figures S6D and S6F). This effect was reversed upon treatment with GDF15Nab, FGFRi, and recombinant IGFBP-2/3 (Figures S6F). Of note, PC3-shTIMP1 treated with docetaxel and subsequently co-cultured with PC3-mCherry cells were capable to

(E) Bar plot represents percentage of lung metastases in all four experimental groups of mice, shCtrl, shCtrl + docetaxel, shTIMP1, and shTIMP1 + docetaxel, n = 5 per group.

(F) Representative IHC images of lung metastases in all four groups of mice at 5 \times magnification. Dotted circles represent metastatic lesions marked by “m” in the lung tissues labeled “l.” Scale bars, 500 μ m.

(G) Bar graph represents the average of metastatic lesions in lungs in the aforementioned groups.

(H) Bar plot represents the percentage of kidney metastases represented in all four groups of mice, shCtrl alone, shCtrl + docetaxel, shTIMP1, and shTIMP1 + docetaxel, n = 5.

(I) Representative IHC images of kidney metastases in all four groups of mice (1 \times). Dotted circles represent metastatic lesions marked by “m” in the kidney tissue labeled “k.” Scale bars, 1 mm.

(J) Bar graph represents an average area in percentage of metastatic lesions within the kidney in the aforementioned groups, n = 5.

(K) Timeline of the experimental metastases model using shTIMP1 PC3-luciferase cells (PC3-luc) in NSG mice treated with vehicle, ABT263, docetaxel, and docetaxel + ABT263.

(L) Representative BLI of shTIMP1 PC3-luc cells colonization in NSG mice with respective treatments.

(M) Relative fold change in bioluminescence signal of total flux in mice with the respective treatments: one-way ANOVA multiple comparison test (Tukey’s test), n = 5.

(N) Percentage of lung metastases in all four groups of mice treated with vehicle, ABT263, docetaxel, and docetaxel + ABT263, n = 5.

(O) Percentage of kidney metastases represented in all four groups of mice treated with vehicle, ABT263, docetaxel, and docetaxel + ABT263, n = 5.

(P) Representative IHC images of lung and kidney metastases in all four groups of mice (5 \times and 1 \times magnification, respectively). Dotted circles represent metastatic lesions. Scale bars, 500 μ m and 1 mm, respectively.

(Q) Bar graph represents the average of metastatic lesions in lungs in the aforementioned groups.

(R) Bar graph represents the average of metastatic lesions in kidney in the aforementioned groups.

All p values were determined by Student’s t test (unpaired two-tailed) unless mentioned otherwise, n.s., not significant; *p < 0.05, **p < 0.01, ***p < 0.001, ****p < 0.0001. Data are represented as mean \pm SEM. See also Figure S4.

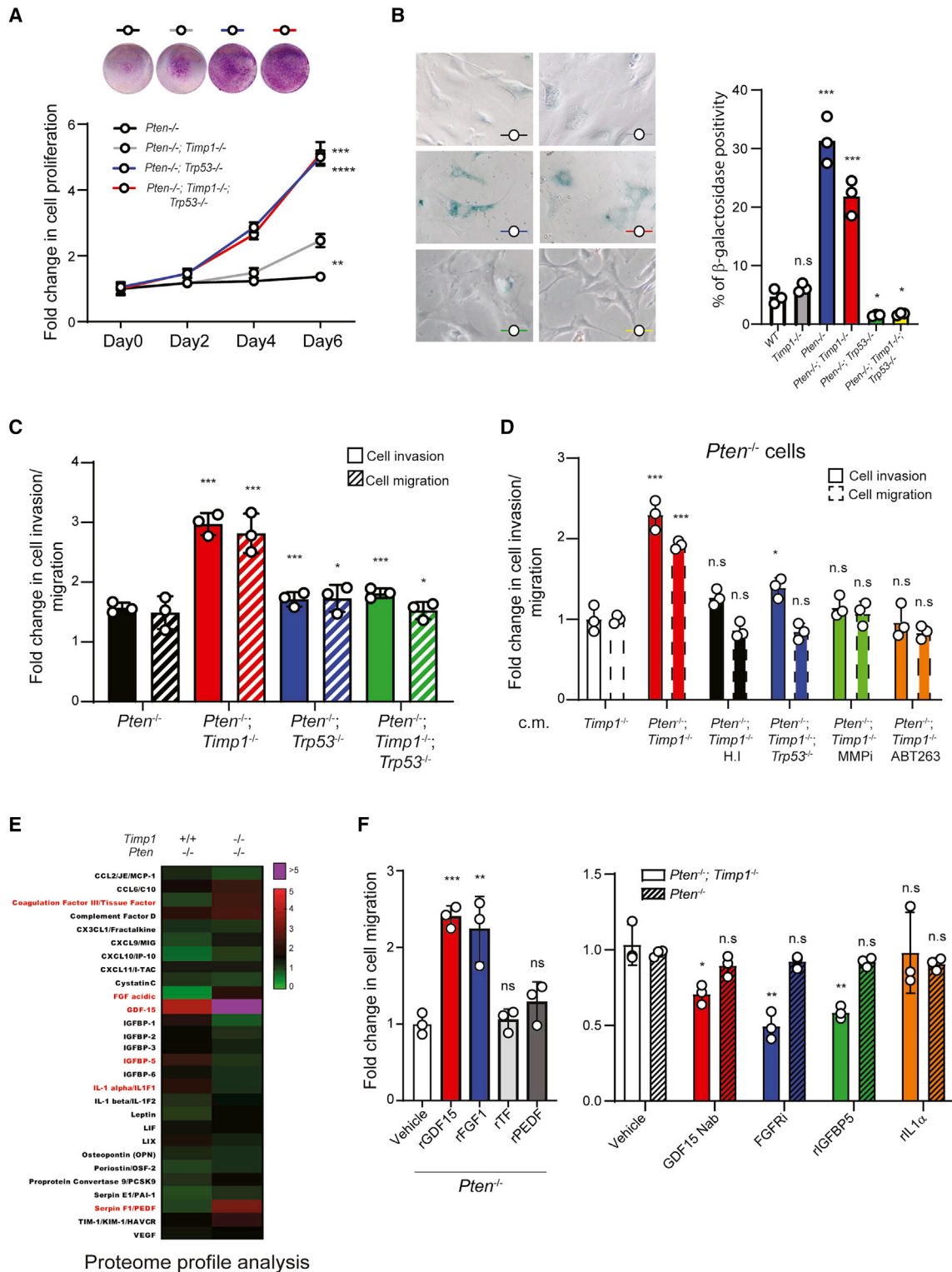


Figure 5. *Timp1*-Loss Reprogrammed SASP of *Pten*-Null Cells to Promote Cell Invasion and Migration

(A) Representative crystal violet staining images of *Pten*^{-/-}, *Pten*^{-/-}; *Timp1*^{-/-}, *Pten*^{-/-}; *Trp53*^{-/-}, and *Pten*^{-/-}; *Trp53*^{-/-}; *Timp1*^{-/-} mouse embryonic fibroblasts (upper panel) with relative fold change in cell proliferation (lower panel).

(B) Representative images of SA-β-gal in the aforementioned genotypes (left panel) with quantification in percentage of staining (right panel), n = 3 per genotype.

(C) Bar graph represents relative fold change in cell invasion and migration of *Pten*^{-/-}, *Pten*^{-/-}; *Timp1*^{-/-}, *Pten*^{-/-}; *Trp53*^{-/-}, and *Pten*^{-/-}; *Timp1*^{-/-}; *Trp53*^{-/-} cells, normalized to their own respective proliferation index, n = 3 per genotype.

(legend continued on next page)

enhance cell proliferation in PC3-mCherry cells. This effect was reverted by ABT263 treatment in PC3-sh*TIMP1* cells (Figures S6G–S6I). In sum, these results demonstrate that senescent *PTEN*; *TIMP1* double null cells promote enhanced cell migration in non-senescent mouse and human tumor cells by acting in a paracrine manner.

TIMP1-Loss Correlates with PTEN-Loss in Advanced and Metastatic Prostate Tumors

Next, we determined the clinical relevance of *TIMP1*-loss in patients affected by prostate cancer by analyzing human prostate cancer tissue microarray (TMA) of 529 cases. While the majority of primary tumors samples stained positive for *TIMP1*, metastatic tumor samples (96%) displayed no positivity for *TIMP1* (Figures 6A and B). In addition, patients with low/negative *TIMP1* levels had a decreased overall and cancer-specific survival when compared with patients with high/positive *TIMP1* levels in the tumors (Figures S7A). These data were also confirmed by bioinformatic analysis (Figures S7B) and are consistent with a role for *TIMP1* in limiting tumor progression in human prostate cancer. RNA sequencing analysis of prostate tumor areas (TA1 and TA2) and adjacent normal prostate tissues showed decreased levels of *TIMP1* in the tumor areas (Figures 6C and 6D). This result was confirmed in a separate dataset showing that *TIMP1* mRNA levels were found to be downregulated in prostate cancer compared with its normal counterpart and tumors of different tissue origin (Figure S7C). Moreover, prostate tumors did not display amplification, deep deletion or mutations for *TIMP1* (Figure S7C). Together, these data indicate that *TIMP1*-loss in prostate cancer is associated with the downregulation of *TIMP1* mRNA levels. The lack of genetic alterations in the *TIMP1* locus suggested an epigenetic silencing. Coherently with this hypothesis, we found that the *TIMP1* promoter was significantly and exclusively methylated in prostate tumors compared with a wide range of malignancies (Figure S7D). Of note, *TIMP1* promoter methylation was detected in both primary and metastatic tumors in different independent datasets (Figures 6E and S7E). Moreover, bioinformatics analysis revealed a positive correlation between *PTEN* and *TIMP1* at the gene expression levels (Figure 6F). This was confirmed by IHC analysis in a prostate cancer TMA of 611 cases. Decreased protein levels of *TIMP1* and *PTEN* were predominantly found in metastatic prostate cancer samples. Indeed, the percentage of cases with double-negative staining increased from 12% in primary prostate tumors to 61% in metastatic tumor samples (Figures 6G and 6H). Of note, *TIMP1* promoter methylation was significantly associated with decreased expression of *TIMP1* and *PTEN* and increased

rate of *PTEN* deletion/mutation (Figures 6I and S7F). Taken together, these results demonstrate that in prostate cancer, *TIMP1* is lost at mRNA level due to promoter methylation and significantly correlates with loss of *PTEN*.

TIMP1 Loss Is Associated with Lack of Responsiveness to Docetaxel Treatment in Patients with Localized High-Grade Prostate Cancer

In light of these findings, we next aimed to validate these findings in a human-relevant clinical setting. For this reason, we took advantage of a prospective study (TAX2501) in which adjuvant docetaxel treatment was administered immediately after surgery in patients with high-risk localized prostate cancer that underwent radical prostatectomy (Antonarakis et al., 2012). From 77 patients enrolled in the TAX2501 trial, 57 tumor specimens were obtained that were suitable for IHC analysis. The TAX2501 study was designed with the primary endpoint being progression-free survival defined as the first of serological progression, clinical progression or radiographic progression of the disease. In this clinical study, 26% of patients (n = 15) responded to docetaxel treatment, while 74% of patients experienced disease progression as defined above (n = 42) (Antonarakis et al., 2012). IHC analysis revealed that the majority of patients (12 out of 15) with tumors expressing high levels of *TIMP1* responded to adjuvant docetaxel treatment when compared with patients with tumor expressing low levels of *TIMP1* (26 out of 42) (Figures 7A and 7B). We next determined whether the combined loss of *PTEN* and *TIMP1* could predict a worst clinical outcome. The combined loss of *PTEN* and *TIMP1* was found in the majority of non-responder patients (23 out of 42) with inferior disease-free survival compared with those with high levels of *PTEN* and *TIMP1* (Figures 7C and 7D). These results were consistent with the data obtained from our GEMMs and display an association between a combined loss of *PTEN* and *TIMP1* and a lack of responsiveness to docetaxel treatment with inferior clinical outcomes.

DISCUSSION

Effective clinical management of metastatic CaP is challenging due to a limited understanding of the genetic and cellular elements governing disease progression. Thus, determining the underlying mechanisms of metastatic transition in primary tumors would help develop a rationale to prevent the emergence of metastatic CaP, thus keeping the disease at bay (Steeg, 2016). Recent studies have raised the possibility that senescent cells in tumors, while initially restricting tumorigenesis, may promote tumor progression and metastases at a late stage (Camphausen et al., 2001; Demaria et al., 2017; Kim et al.,

(D) Bar graph represents relative fold change in invasion and migration of *Pten*^{-/-} cells 48 h post-incubation with condition medium (c.m.) harvested from *Timp1*^{-/-}, *Pten*^{-/-}; *Timp1*^{-/-}, and *Pten*^{-/-}; *Timp1*^{-/-}; *Trp53*^{-/-} cells along with c.m. from *Pten*^{-/-}; *Timp1*^{-/-} cells treated with Pan-MMP inhibitor (MMPi), ABT263, or heat-inactivated c.m. (H.I.), n = 3.

(E) Proteome profile analysis of c.m. derived from *Pten*^{-/-} and *Pten*^{-/-}; *Timp1*^{-/-} cells of MMP substrate proteins. Range of the of protein expression values (fold change) is represented by the color palette. Red color represents the higher expression and green represents the lower expression of the proteins. Violet color represents the highest expression, >5 fold change. Highlighted in red are the differentially expressed factors.

(F) Bar graph (left) represents fold change in migration of *Pten*^{-/-} cells upon treatment with recombinants for GDF-15, FGF1, TF, and PEDF. Bar graph (right) represents fold change in migration of *Pten*^{-/-} and *Pten*^{-/-}; *Timp1*^{-/-} cells upon treatment with GDF15Nab, FGFRI, rIGFBP-5, and rIL1- α , n = 3.

The p values were determined by Student's t test (unpaired two-tailed), n.s., not significant; *p < 0.05, **p < 0.01, ***p < 0.001, ****p < 0.0001. Data are represented as mean \pm SEM. See also Figures S5 and S6.

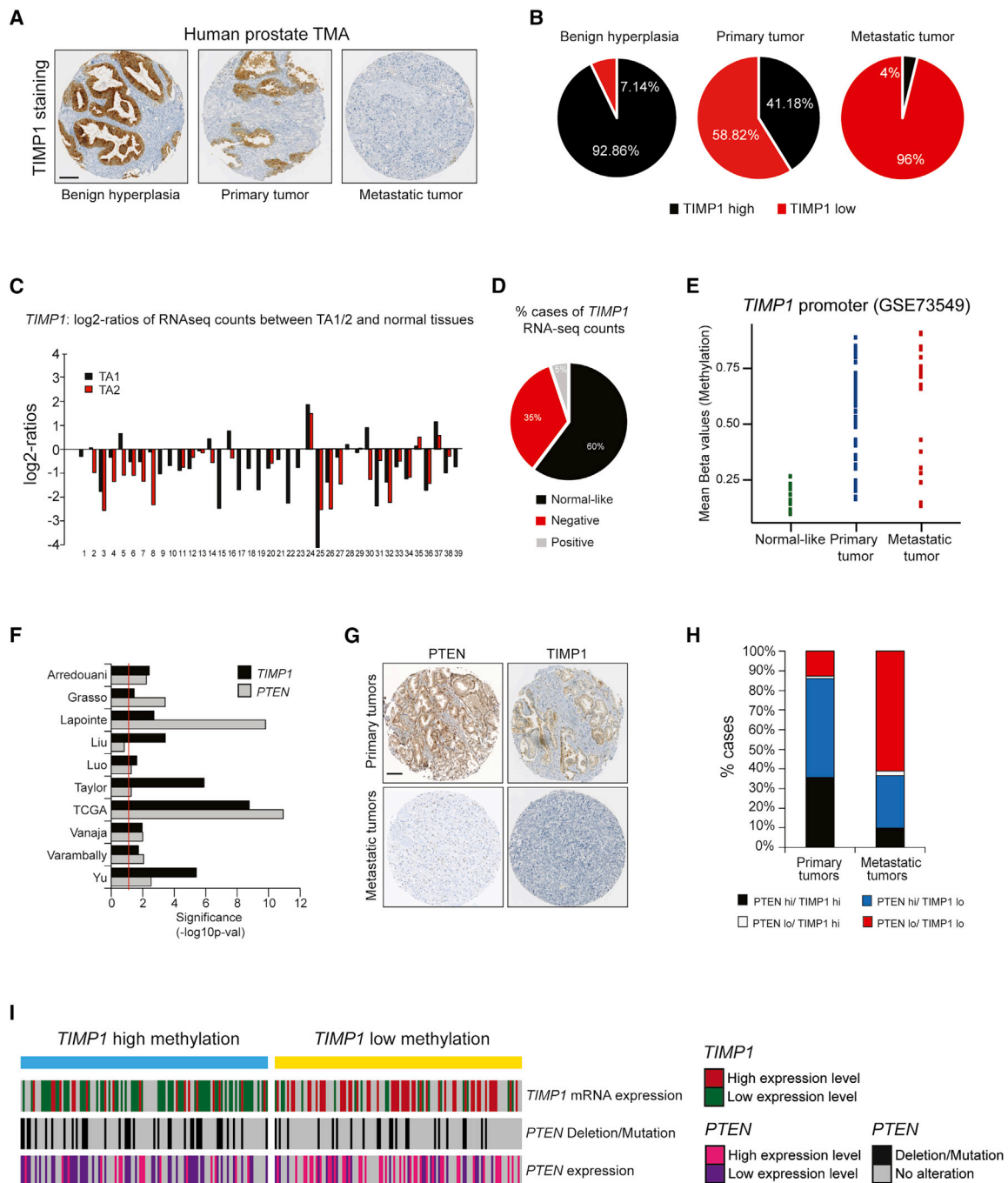


Figure 6. TIMP1 Is Lost in Advanced and Metastatic Prostate Tumors Due to Promoter Methylation

(A) Representative images of TIMP1 staining in human prostate cancer tissue microarray (TMA), n = 529. Scale bar, 100 μ m.
 (B) Pie charts displaying quantification in percentage of TIMP1 staining in 529 cases in benign hyperplasia, primary, and metastatic tumors.
 (C) TIMP1 log₂ ratios of RNA sequencing counts between tumor areas (TA) 1 and 2 compared with those in normal adjacent tissues within the same tumor samples, n = 39.
 (D) Pie chart represents the quantification of TIMP1 levels as shown in (C). The fraction in black represents normal levels of TIMP1, that in red represents TIMP1-negative tissues, while that in gray represents TIMP1-positive tissues.
 (E) Graph representing mean methylation beta values of all CpG sites located in the promoter region of the TIMP1 gene for adjacent normal (in black), primary tumors (in blue), and metastatic tumors (in red) from the GEO: GSE73549 dataset (Mundbjerg et al., 2017).
 (F) Bar plot enlists prostate cancer datasets demonstrating a positive correlation between the expressions of TIMP1 and PTEN.

(legend continued on next page)

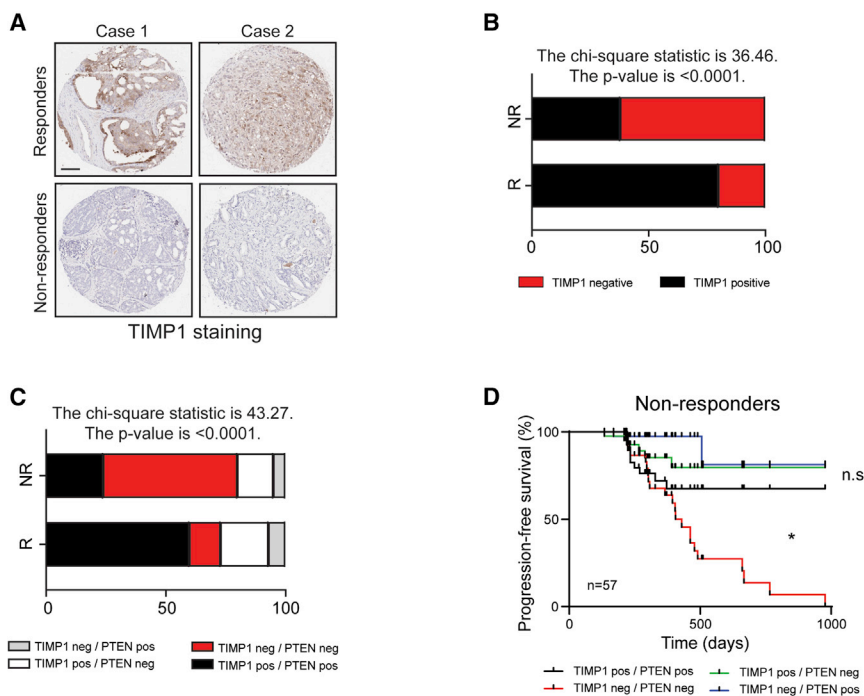


Figure 7. Loss of Intra-tumoral PTEN and TIMP1 Correlated with Non-responsiveness to Docetaxel Treatment and Inferior Clinical Outcomes in Patients

(A) Representative images of TIMP1 staining in two individual cases of human prostate cancer TMA cases from the TAX2501 study (Antonarakis et al., 2012), $n = 57$. Scale bar, 100 μm .

(B) Bar plot representing the percentage of cases with TIMP1 protein expression (positive or negative) in tumor samples from responders (R) versus non-responders (NR).

(C) Bar plot representing the percentage of cases with different combinations of TIMP1 and PTEN expression (positive or negative) in tumor samples from responders (R) versus non-responders (NR).

(D) Progression-free survival curves constructed and compared by Mantel-Cox log rank test in four categories defined by TIMP1 and PTEN expression (positive and negative).

TIMP1 in therapy-resistance and tumor relapse. These data were validated in an experimental metastases model where TIMP1^{+/+} and TIMP1^{-/-} human

2017). This coexisting dichotomy remains unclear due to the lack of evidence on the mechanism by which senescent tumor cells initiate metastases (Coppe et al., 2010a). Here, we identified TIMP1 as a critical regulator of initiation and promotion of CaP metastases by switching senescence from tumor-suppressive to a tumor-promoting response. Using GEMMs, we demonstrate that the genetic inactivation of *Timp1* decreases the survival of mice with enhanced metastases, only in senescent *Pten*^{pc-/-} but not in non-senescent *Pten*^{pc-/-}; *Trp53*^{pc-/-} mice. Of note, *Timp1* inactivation alone did not show any signs of tumor initiation. Importantly, although *Timp1*-loss activated MMPs to a similar extent in both *Pten*^{pc-/-} and *Pten*^{pc-/-}; *Trp53*^{pc-/-} tumors, metastases were observed only in mice bearing senescent tumors. Furthermore, we unraveled the potential role of senescence in metastases initiation by targeting senescent *Pten*^{pc-/-}; *Timp1*^{-/-} tumor cells using the Bcl2 inhibitor ABT263, a senolytic compound used for the treatment of aging (Calcinotto et al., 2019; Chang et al., 2016; Demaria et al., 2017). Of note, single-cell sequencing in prostate tumors showed that Bcl2 was selectively upregulated in senescent tumor cells. Consequently, ABT263 treatment depleted senescent tumor cells in *Pten*^{pc-/-}; *Timp1*^{-/-} mice, thereby impairing metastases formation. In line with these findings, we found that TIS caused tumor regression in mice bearing *Timp1*-proficient tumors, but it accelerated metastases formation in mice bearing *Timp1*-deficient tumors. Resistance to docetaxel treatment with antedated metastases unveils a previously unknown function of

prostate tumor cells were injected in recipient mice. While TIMP1^{-/-} cells showed an increased capability to form metastases when treated with docetaxel, concomitant administration of ABT263 resulted in the clearance of senescent tumor cells and in the prevention of metastases. Mechanistically, we discovered that *TIMP1* inactivation in senescent tumor cells activates MMPs changing the SASP. Previous evidences demonstrate that MMPs can regulate the levels of several secreted factors that affect tumor cell migration (Klein and Bischoff, 2011; Nagase et al., 2006; Page-McCaw et al., 2007; Rodriguez et al., 2010; Visse and Nagase, 2003). Proteome profiling analysis performed on the senescent secretome of mouse and human TIMP1-deficient tumor cells treated with docetaxel showed increased levels of GDF-15, FGF1, and decreased levels of IGFBP-5, three known regulators of cell migration (Suyama et al., 2002).

Of great relevance for the clinic, we found that *TIMP1*-loss is frequently associated with epigenetic silencing and *PTEN*-loss in advanced and metastatic CaP and that patients with tumors expressing low levels of PTEN and TIMP1 respond poorly to docetaxel treatment and show a shorter disease-free survival. Altogether, these results validate our study in a relevant human setting. Given the *in vivo* data in GEMMs and the clinical evidence in patients, we believe that TIS should be administered with caution in CaP patients with *TIMP1*-null genetic background. These data may also explain recent clinical findings demonstrating the lack of efficacy of docetaxel when administered in an adjuvant setting (Petrylak et al., 2004; Tannock

(G) Representative images of human TMA samples stained for PTEN and TIMP1 in primary and metastatic tumor cases. Scale bar, 100 μm .

(H) Bar plot representing percentage of cases with PTEN and TIMP1 protein expression in primary and metastatic tumor samples, $n = 611$.

(I) Heatmap showing *TIMP1* and *PTEN* expressions and *PTEN* deletion/mutation in *TIMP1* high versus low methylated groups of patients. Analysis was performed using a TCGA bio-link package in R-bioconductor (Colaprico et al., 2016).

See also Figure S7.

et al., 2004). In sum, TIMP1 can be used as a biomarker to guide therapeutic interventions in patients affected by metastatic prostate cancer, sparing some patients from the unnecessary toxicities of chemotherapy (Kellokumpu-Lehtinen et al., 2012). Importantly, our study vouches for “senolytic medicine” in cancer treatment, especially in combating metastatic transition in tumors with TIMP1 deficiency, without limiting its translational value only for the treatment of aging-related pathologies (Chang et al., 2016).

STAR★METHODS

Detailed methods are provided in the online version of this paper and include the following:

- **KEY RESOURCES TABLE**
- **RESOURCE AVAILABILITY**
 - Lead Contact
 - Materials Availability
 - Data and Code Availability
- **EXPERIMENTAL MODEL AND SUBJECT DETAILS**
 - Mouse Models
 - MEFs Production and Cell Culture
 - Human Tissue Microarray (TMA)
 - Prostate Cancer Cell Culture
- **METHOD DETAILS**
 - Transgenic Mouse Model Treatments
 - Transgenic Mouse Model Bone Marrow Reconstitution
 - Generation *In Vivo* Experimental Metastatic Model
 - Generation of Pten KO MEFs
 - Generation of shTIMP1 Human Prostate Cancer Cell Line
 - Immunohistochemistry (IHC) and Immunofluorescence (IF)
 - Senescence associated β -galactosidase (SA- β -gal) Assay
 - Single Molecule Fluorescent In-Situ Hybridization
 - Single Cell Sequencing Analysis
 - Proliferation Assays
 - Invasion and Migration Assay
 - Co-culture Experiment
 - Condition Media and Protein Profiler Assay
 - Recombinant Experiment
 - Western Blot
 - Antibodies
 - Gelatin-Zymography
 - PCR Genotyping
 - Quantitative Real-Time PCR (qRT-PCR)
 - Gene Expression Profiling
 - TCGA and GEO DNA Methylation Analysis
 - RNA-Seq Dataset Analysis
- **QUANTIFICATION AND STATISTICAL ANALYSIS**

SUPPLEMENTAL INFORMATION

Supplemental Information can be found online at <https://doi.org/10.1016/j.ccell.2020.10.012>.

ACKNOWLEDGMENTS

We acknowledge all the members of Alimonti lab and IOR/IRB institutes. This work was supported by ERC consolidator (683136), a Swiss Cancer League (KFS4267-08-2017) grant, the Dr. Josef Steiner Foundation, a Swiss Card-Onco-Grant of Alfred and Annemarie von Sick grant, and the Helmut Horten Foundation, SNSF (310030_176045), PCUK (RIA15-ST2-018), and IBSA Foundation.

AUTHOR CONTRIBUTIONS

Conceptualization, A.A., I.G., and A.R.; Writing – Original Draft, A.A., I.G., and A.R.; *In Vivo* and *In Vitro* Experiments, I.G., A.R., M.C., M.D., E.P., G.A., N.P., D.B. and A.R.E.; Bioinformatics, M.T. and R.G.-E.; Clinical Samples, S.M., M.L., R.S.-T., G.E., J.H.R., S.D., H.M., P.W., A.M.D.M., and E.S.A.; smFISH, C.B. and A.E.M.

DECLARATION OF INTERESTS

A.A. is a cofounder of and owns stock in OncoSense and is an inventor of the patent WO2019142095A1. E.S.A. is a paid consultant/advisor to Janssen, Astellas, Sanofi, Dendreon, Pfizer, Amgen, Eli-Lilly, Bayer, AstraZeneca, Bristol-Myers Squibb, Clovis, and Merck; he has received research funding to his institution from Janssen, Johnson & Johnson, Sanofi, Dendreon, Genentech, Novartis, Constellation, Bristol-Myers Squibb, AstraZeneca, Clovis, and Merck; and he is the co-inventor of a patented biomarker technology that has been licensed to QIAGEN.

Received: February 25, 2020
Revised: September 12, 2020
Accepted: October 9, 2020
Published: November 12, 2020

REFERENCES

- Antonarakis, E.S., Keizman, D., Zhang, Z., Gurel, B., Lotan, T.L., Hicks, J.L., Fedor, H.L., Carducci, M.A., De Marzo, A.M., and Eisenberger, M.A. (2012). An immunohistochemical signature comprising PTEN, MYC, and Ki67 predicts progression in prostate cancer patients receiving adjuvant docetaxel after prostatectomy. *Cancer* 118, 6063–6071.
- Benjamini, Y., and Hochberg, Y. (1995). Controlling the false discovery rate: a practical and powerful approach to multiple testing. *J. R. Stat. Soc. Ser. B (Methodological)* 57, 289–300.
- Calcinotto, A., Kohli, J., Zagato, E., Pellegrini, L., Demaria, M., and Alimonti, A. (2019). Cellular senescence: aging, cancer, and injury. *Physiol. Rev.* 99, 1047–1078.
- Camphausen, K., Moses, M.A., Beecken, W.D., Khan, M.K., Folkman, J., and O'Reilly, M.S. (2001). Radiation therapy to a primary tumor accelerates metastatic growth in mice. *Cancer Res.* 61, 2207–2211.
- Chang, J., Wang, Y., Shao, L., Laberge, R.M., Demaria, M., Campisi, J., Janakiraman, K., Sharpless, N.E., Ding, S., Feng, W., et al. (2016). Clearance of senescent cells by ABT263 rejuvenates aged hematopoietic stem cells in mice. *Nat. Med.* 22, 78–83.
- Chen, S., Huang, T., Zhou, Y., Han, Y., Xu, M., and Gu, J. (2017). AfterQC: automatic filtering, trimming, error removing and quality control for fastq data. *BMC Bioinformatics* 18, 80.
- Chen, Z., Trotman, L.C., Shaffer, D., Lin, H.K., Dotan, Z.A., Niki, M., Koutcher, J.A., Scher, H.I., Ludwig, T., Gerald, W., et al. (2005). Crucial role of p53-dependent cellular senescence in suppression of Pten-deficient tumorigenesis. *Nature* 436, 725–730.
- Colaprico, A., Silva, T.C., Olsen, C., Garofano, L., Cava, C., Garolini, D., Sabedot, T.S., Malta, T.M., Pagnotta, S.M., Castiglioni, I., et al. (2016). TCGAAbiolinks: an R/Bioconductor package for integrative analysis of TCGA data. *Nucleic Acids Res.* 44, e71.
- Collado, M., Gil, J., Efeyan, A., Guerra, C., Schuhmacher, A.J., Barradas, M., Benguria, A., Zaballos, A., Flores, J.M., Barbacid, M., et al. (2005). Tumour biology: senescence in premalignant tumours. *Nature* 436, 642.

- Coppe, J.P., Desprez, P.Y., Krtolica, A., and Campisi, J. (2010a). The senescence-associated secretory phenotype: the dark side of tumor suppression. *Annu. Rev. Pathol.* **5**, 99–118.
- Coppe, J.P., Patil, C.K., Rodier, F., Krtolica, A., Beausejour, C.M., Parrinello, S., Hodgson, J.G., Chin, K., Desprez, P.Y., and Campisi, J. (2010b). A human-like senescence-associated secretory phenotype is conserved in mouse cells dependent on physiological oxygen. *PLoS One* **5**, e9188.
- Demaria, M., O'Leary, M.N., Chang, J., Shao, L., Liu, S., Alimirah, F., Koenig, K., Le, C., Mitin, N., Deal, A.M., et al. (2017). Cellular senescence promotes adverse effects of chemotherapy and cancer relapse. *Cancer Discov.* **7**, 165–176.
- Di Mitri, D., Toso, A., Chen, J.J., Sarti, M., Pinton, S., Jost, T.R., D'Antuono, R., Montani, E., Garcia-Escudero, R., Guccini, I., et al. (2014). Tumour-infiltrating Gr-1+ myeloid cells antagonize senescence in cancer. *Nature* **515**, 134–137.
- Dobin, A., Davis, C.A., Schlesinger, F., Drenkow, J., Zaleski, C., Jha, S., Batut, P., Chaisson, M., and Gingeras, T.R. (2013). STAR: ultrafast universal RNA-seq aligner. *Bioinformatics* **29**, 15–21.
- Faget, D.V., Ren, Q., and Stewart, S.A. (2019). Unmasking senescence: context-dependent effects of SASP in cancer. *Nat. Rev. Cancer* **19**, 439–453.
- Farack, L., Golan, M., Egozi, A., Dezorella, N., Bahar Halpern, K., Ben-Moshe, S., Garzilli, I., Toth, B., Roitman, L., Krizhanovsky, V., and Itzkovitz, S. (2019). Transcriptional heterogeneity of beta cells in the intact pancreas. *Dev Cell* **48**, 115–125.e4.
- Fridlender, Z.G., Sun, J., Mishalian, I., Singhal, S., Cheng, G., Kapoor, V., Horng, W., Fridlender, G., Bayuh, R., Worthen, G.S., and Albelda, S.M. (2012). Transcriptomic analysis comparing tumor-associated neutrophils with granulocytic myeloid-derived suppressor cells and normal neutrophils. *PLoS One* **7**, e31524.
- Garcia-Alcalde, F., Okonechnikov, K., Carbonell, J., Cruz, L.M., Gotz, S., Tarazona, S., Dopazo, J., Meyer, T.F., and Conesa, A. (2012). Qualimap: evaluating next-generation sequencing alignment data. *Bioinformatics* **28**, 2678–2679.
- Gong, Y., Chippada-Venkata, U.D., Galsky, M.D., Huang, J., and Oh, W.K. (2015). Elevated circulating tissue inhibitor of metalloproteinase 1 (TIMP-1) levels are associated with neuroendocrine differentiation in castration resistant prostate cancer. *Prostate* **75**, 616–627.
- Gorgoulis, V., Adams, P.D., Alimonti, A., Bennett, D.C., Bischof, O., Bishop, C., Campisi, J., Collado, M., Evangelou, K., Ferbeyre, G., et al. (2019). Cellular senescence: defining a path forward. *Cell* **179**, 813–827.
- Grimm, D., Bauer, J., Wise, P., Kruger, M., Simonsen, U., Wehland, M., Infanger, M., and Corydon, T.J. (2019). The role of SOX family members in solid tumours and metastasis. *Semin. Cancer Biol.* <https://doi.org/10.1016/j.semcancer.2019.03.004>.
- Harrow, J., Frankish, A., Gonzalez, J.M., Tapanari, E., Diekhans, M., Kokocinski, F., Aken, B.L., Barrell, D., Zadissa, A., Searle, S., et al. (2012). GENCODE: the reference human genome annotation for the ENCODE Project. *Genome Res.* **22**, 1760–1774.
- Itzkovitz, S., Lyubimova, A., Blat, I.C., Maynard, M., van Es, J., Lees, J., Jacks, T., Clevers, H., and van Oudenaarden, A. (2011). Single-molecule transcript counting of stem-cell markers in the mouse intestine. *Nat. Cell Biol.* **14**, 106–114.
- Jackson, H.W., Defamie, V., Waterhouse, P., and Khokha, R. (2017). TIMPs: versatile extracellular regulators in cancer. *Nat. Rev. Cancer* **17**, 38–53.
- Kastenhuber, E.R., and Lowe, S.W. (2017). Putting p53 in context. *Cell* **170**, 1062–1078.
- Kellokumpu-Lehtinen, P.L., Hjalml-Eriksson, M., Thellenberg-Karlsson, C., Astrom, L., Franzen, L., Marttila, T., Seke, M., Taalikka, M., Ginman, C., and Spcg. (2012). Toxicity in patients receiving adjuvant docetaxel + hormonal treatment after radical radiotherapy for intermediate or high-risk prostate cancer: a preplanned safety report of the SPCG-13 trial. *Prostate Cancer Prostatic Dis.* **15**, 303–307.
- Kessenbrock, K., Plaks, V., and Werb, Z. (2010). Matrix metalloproteinases: regulators of the tumor microenvironment. *Cell* **141**, 52–67.
- Kim, Y.H., Choi, Y.W., Lee, J., Soh, E.Y., Kim, J.H., and Park, T.J. (2017). Senescent tumor cells lead the collective invasion in thyroid cancer. *Nat. Commun.* **8**, 15208.
- Klein, T., and Bischoff, R. (2011). Physiology and pathophysiology of matrix metalloproteinases. *Amino Acids* **41**, 271–290.
- Kuroda, N., Masuya, M., Tawara, I., Tsuboi, J., Yoneda, M., Nishikawa, K., Kageyama, Y., Hachiya, K., Ohishi, K., Miwa, H., et al. (2019). Infiltrating CCR2(+) monocytes and their progenies, fibrocytes, contribute to colon fibrosis by inhibiting collagen degradation through the production of TIMP-1. *Sci. Rep.* **9**, 8568.
- Laberge, R.M., Awad, P., Campisi, J., and Desprez, P.Y. (2012). Epithelial-mesenchymal transition induced by senescent fibroblasts. *Cancer Microenvironment* **5**, 39–44.
- Lecot, P., Alimirah, F., Desprez, P.Y., Campisi, J., and Wiley, C. (2016). Context-dependent effects of cellular senescence in cancer development. *Br. J. Cancer* **114**, 1180–1184.
- Liberzon, A., Birger, C., Thorvaldsdottir, H., Ghandi, M., Mesirov, J.P., and Tamayo, P. (2015). The Molecular Signatures Database (MSigDB) hallmark gene set collection. *Cell Syst.* **1**, 417–425.
- Liberzon, A., Subramanian, A., Pinchback, R., Thorvaldsdottir, H., Tamayo, P., and Mesirov, J.P. (2011). Molecular signatures database (MSigDB) 3.0. *Bioinformatics* **27**, 1739–1740.
- Litwin, M.S., and Tan, H.J. (2017). The diagnosis and treatment of prostate cancer: a review. *JAMA* **317**, 2532–2542.
- Livak, K.J., and Schmittgen, T.D. (2001). Analysis of relative gene expression data using real-time quantitative PCR and the 2^{-ΔΔC_T}(T). *Methods* **4**, 402–408.
- Love, M.I., Huber, W., and Anders, S. (2014). Moderated estimation of fold change and dispersion for RNA-seq data with DESeq2. *Genome Biol.* **15**, 550.
- Lyubimova, A., Itzkovitz, S., Junker, J.P., Fan, Z.P., Wu, X., and van Oudenaarden, A. (2013). Single-molecule mRNA detection and counting in mammalian tissue. *Nat. Protoc.* **8**, 1743–1758.
- Mundbjerg, K., Chopra, S., Alemozaffar, M., Duymich, C., Lakshminarasimhan, R., Nichols, P.W., Aron, M., Siegmund, K.D., Ukimura, O., Aron, M., et al. (2017). Identifying aggressive prostate cancer foci using a DNA methylation classifier. *Genome Biol.* **18**, 3.
- Nagase, H., Visse, R., and Murphy, G. (2006). Structure and function of matrix metalloproteinases and TIMPs. *Cardiovasc. Res.* **69**, 562–573.
- Page-McCaw, A., Ewald, A.J., and Werb, Z. (2007). Matrix metalloproteinases and the regulation of tissue remodelling. *Nat. Rev. Mol. Cell Biol.* **8**, 221–233.
- Petrylak, D.P., Tangen, C.M., Hussain, M.H., Lara, P.N., Jr., Jones, J.A., Taplin, M.E., Burch, P.A., Berry, D., Moynour, C., Kohli, M., et al. (2004). Docetaxel and estramustine compared with mitoxantrone and prednisone for advanced refractory prostate cancer. *N. Engl. J. Med.* **351**, 1513–1520.
- Rawla, P. (2019). Epidemiology of prostate cancer. *World J. Oncol.* **10**, 63–89.
- Rodriguez, D., Morrison, C.J., and Overall, C.M. (2010). Matrix metalloproteinases: what do they not do? New substrates and biological roles identified by murine models and proteomics. *Biochim. Biophys. Acta* **1803**, 39–54.
- Sieben, C.J., Sturmlechner, I., van de Sluis, B., and van Deursen, J.M. (2018). Two-step senescence-focused cancer therapies. *Trends Cell Biol.* **28**, 723–737.
- Steeg, P.S. (2016). Targeting metastasis. *Nat. Rev. Cancer* **16**, 201–218.
- Suyama, K., Shapiro, I., Guttman, M., and Hazan, R.B. (2002). A signaling pathway leading to metastasis is controlled by N-cadherin and the FGF receptor. *Cancer Cell* **2**, 301–314.
- Tanaka, H., Kono, E., Tran, C.P., Miyazaki, H., Yamashiro, J., Shimomura, T., Fazli, L., Wada, R., Huang, J., Vessella, R.L., et al. (2010). Monoclonal antibody targeting of N-cadherin inhibits prostate cancer growth, metastasis and castration resistance. *Nat. Med.* **16**, 1414–1420.
- Tannock, I.F., de Wit, R., Berry, W.R., Horti, J., Pluzanska, A., Chi, K.N., Oudard, S., Theodore, C., James, N.D., Turesson, I., et al. (2004). Docetaxel plus prednisone or mitoxantrone plus prednisone for advanced prostate cancer. *N. Engl. J. Med.* **351**, 1502–1512.

Toso, A., Revandkar, A., Di Mitri, D., Guccini, I., Proietti, M., Sarti, M., Pinton, S., Zhang, J., Kalathur, M., Civenni, G., et al. (2014). Enhancing chemotherapy efficacy in Pten-deficient prostate tumors by activating the senescence-associated antitumor immunity. *Cell Rep.* *9*, 75–89.

Umbehr, M., Kessler, T.M., Sulser, T., Kristiansen, G., Probst, N., Steurer, J., and Bachmann, L.M. (2008). ProCOC: the Prostate Cancer Outcomes Cohort study. *BMC Urol.* *8*, 9.

van Dijk, D., Sharma, R., Nainys, J., Yim, K., Kathail, P., Carr, A.J., Burdziak, C., Moon, K.R., Chaffer, C.L., Pattabiraman, D., et al. (2018). Recovering gene interactions from single-cell data using data diffusion. *Cell* *174*, 716–729 e727.

Visse, R., and Nagase, H. (2003). Matrix metalloproteinases and tissue inhibitors of metalloproteinases: structure, function, and biochemistry. *Circ. Res.* *92*, 827–839.

Wang, L., Wang, S., and Li, W. (2012). RSeQC: quality control of RNA-seq experiments. *Bioinformatics* *28*, 2184–2185.

Wang, Y., Ding, Y., Guo, N., and Wang, S. (2019). MDSCs: key criminals of tumor pre-metastatic niche formation. *Front. Immunol.* *10*, 172.

Wu, D., and Smyth, G.K. (2012). Camera: a competitive gene set test accounting for inter-gene correlation. *Nucleic Acids Res.* *40*, e133.

Wynn, T.A., and Barron, L. (2010). Macrophages: master regulators of inflammation and fibrosis. *Semin. Liver Dis.* *30*, 245–257.

Xue, W., Zender, L., Miething, C., Dickins, R.A., Hernando, E., Krizhanovskiy, V., Cordon-Cardo, C., and Lowe, S.W. (2007). Senescence and tumour clearance is triggered by p53 restoration in murine liver carcinomas. *Nature* *445*, 656–660.

Zhong, Q., Ruschoff, J.H., Guo, T., Gabrani, M., Schuffler, P.J., Rechsteiner, M., Liu, Y., Fuchs, T.J., Rupp, N.J., Fankhauser, C., et al. (2016). Image-based computational quantification and visualization of genetic alterations and tumour heterogeneity. *Sci. Rep.* *6*, 24146.

STAR★METHODS

KEY RESOURCES TABLE

REAGENT or RESOURCE	SOURCE	IDENTIFIER
Antibodies		
Brilliant Violet 605™ anti-mouse CD45.2 Antibody	Biolegend	Cat# 109841; RRID: AB_2563485
CD45.1 Monoclonal Antibody (A20), APC eBioscience™	Invitrogen	Cat# 17-0453-82; RRID: AB_469398
7-AAD Viability Staining	eBioscience	Cat# 00-6993-42
Goat Anti-Mouse IgG Antibody (H+L), Biotinylated	Vector Laboratories	Cat# BP-9200; RRID: AB_2827937
Goat Anti-Rabbit IgG Antibody (H+L), Biotinylated	Vector Laboratories	Cat# BP-9100; RRID: AB_1958865
CD326 (EpCAM) Monoclonal Antibody (G8.8), FITC, eBioscience™	Invitrogen	Cat# 11-5791-82; RRID: AB_11151709
APC anti-mouse CD45 Antibody	Biolegend	Cat# 103112; RRID: AB_1283450
Anti-Rabbit IgG (H+L), HRP Conjugate	Promega	Cat# W4011; RRID: AB_430833
Anti-Mouse IgG (H+L), HRP Conjugate	Promega	Cat# W4021; RRID: AB_430834
Mouse TIMP-1 Antibody	R&D systems	Cat# AF980; RRID: AB_355759
PTEN Antibody	Cell Signaling Technology	Cat# 9552; RRID: AB_10694066
p53 Antibody (FL-393)	Santa Cruz Biotechnology	Cat# sc-6243; RRID: AB_653753
HSP90 (C45G5) Rabbit mAb	Cell Signaling Technology	Cat# 4877; RRID: AB_2233207
Monoclonal anti-β-Actin Antibody produced in mouse	Sigma	Cat# A2228; RRID: AB_476697
TIMP1 Monoclonal Antibody (F31 P2 A5)	Invitrogen	Cat# MA1-773; RRID: AB_889482
Ki-67, Rabbit Monoclonal Antibody	Lab Vision	Cat# RM-9106-R7; RRID: AB_149920
Recombinant Anti-CDKN2A/p16INK4a antibody [EPR20418]	Abcam	Cat# ab211542
Cleaved Caspase-3 (Asp175) Antibody	Cell Signaling Technology	Cat# 9661; RRID: AB_2341188
Polyclonal Rabbit Anti-Cytokeratin, Wide Spectrum Screening	Dako Agilent	Cat# Z0622; RRID: AB_2650434
Recombinant Anti-Androgen Receptor antibody [EPR1535(2)]	Abcam	Cat# ab133273; RRID: AB_11156085
PTEN Polyclonal Antibody	Invitrogen	Cat# 51-2400; RRID: AB_2336044
Monoclonal Mouse Anti-Human Tissue Inhibitor of Metalloproteinases 1, Clone VT7	Dako Agilent	Cat# M7293
Purified Mouse Anti-N-Cadherin	BD Bioscience	Cat# 610920; RRID: AB_2077527
Goat anti-Mouse IgG (H+L) Cross-Adsorbed Secondary Antibody, Alexa Fluor 594	Invitrogen	Cat# A11005; RRID: AB_141372
Goat anti-Rabbit IgG (H+L) Cross-Adsorbed Secondary Antibody, Alexa Fluor 488	Invitrogen	Cat# A11008; RRID: AB_143165

(Continued on next page)

Continued

REAGENT or RESOURCE	SOURCE	IDENTIFIER
Biological Samples		
Human Tissues Microarrays (TMAs)	Sidney Kimmel Comprehensive Cancer Center, The Johns Hopkins University School of Medicine	N/A
Human Tissues Microarrays (TMAs)	University Hospital Zurich (USZ)	N/A
Chemicals, Peptides, and Recombinant Proteins		
Docetaxel	Teva Pharma AG	Cat# 6984894
ABT263 (Navitoclax)	MedChem express	Cat# HY-10087; CAS: 923564-51-6
Collagenase D from <i>Clostridium histolyticum</i>	Roche	Cat# 11-088858001
DNase I Solution	Thermo Scientific	Cat# 90083
HEPES (1M)	Gibco	Cat# 15630056
OTTIX plus solution	Diapath	Cat# X0076
OTTIX shaper solution	Diapath	Cat# X0096
Eosin G or Y 0.5% alcoholic	Diapath	Cat# C0352
ProLong™ Gold Antifade Mountant with DAPI	Invitrogen	Cat# P36931
ImmPACT® DAB Substrate, Peroxidase (HRP)	Vector laboratories	Cat# SK-4105; RRID: AB_2336520
Bovine Serum Albumin	Sigma-Aldrich	Cat# A2153
Puromycin dihydrochloride from <i>Streptomyces alboniger</i>	Sigma-Aldrich	Cat# P8833
GM6001 MMP Inhibitor	Sigma-Aldrich	Cat# CC1010
Crystal violet solution	Sigma-Aldrich	Cat# V5265
Recombinant Human IGFBP-2 Protein, CF	R&D systems	Cat# 674-B2
Recombinant Mouse IGFBP-3 Protein, CF	R&D systems	Cat# 775-B3
Recombinant Mouse IGFBP-5 Protein, CF	R&D systems	Cat# 578-B5
Recombinant Human GDF-15/MIC-1 (CHO derived)	PeproTech	Cat# 120-28C
Recombinant Murine FGF-acidic	PeproTech	Cat# 450-33A
Recombinant Mouse Coagulation Factor III/Tissue Factor Protein	Novus	Cat# NBP2-52327
Recombinant Mouse Serpin F1/PEDF Protein, CF	R&D systems	Cat# 8295-SF
GDF15 Antibody (aa30-45) Rabbit Polyclonal Antibody	Abgent	Cat# ALS11572
SSR128129E	MedChem express	Cat# HY-15599; CAS: 848318-25-2
RIPA buffer (10X)	Cell Signaling Technology	Cat# 9806
Phenylmethylsulfonyl Fluoride	Calbiochem	Cat# 329-98-06;CAS: 329-98-6
Mayer's Hematoxylin	Diapath	Cat# C0303
Eosin G or Y polychromatic 1% aqueous	Diapath	Cat# C0363
Gelatin from porcine skin	Sigma	Cat# G1890
30% Acrylamide/Bis solution 29:1	Bio-Rad	Cat# 1610156
Zymogram Sample Buffer	Bio-Rad	Cat# 161-0764
10X Zymogram Development Buffer	Bio-Rad	Cat# 161-0766
10X Zymogram Renaturation Buffer	Bio-Rad	Cat# 161-0765
N,N,N,N-Tetramethylethylenediamine	Sigma-Aldrich	Cat# T9281
Critical Commercial Assays		
Proteome Profiler Mouse XL Cytokine Array	R&D systems	Cat# ARY028
Proteome Profiler Human XL Cytokine Array Kit	R&D systems	Cat# ARY022B
Senescence β -Galactosidase Staining Kit	Cell Signaling Technology	Cat# 9860
ImProm-II™ Reverse Transcription System	Promega	Cat# A3800
KAPA SYBR FAST ABI	KAPA Biosystem	Cat# KK4605
Rapid Extract PCR Kit	PCRBIO SYSTEM	Cat# PB10.24

(Continued on next page)

Continued

REAGENT or RESOURCE	SOURCE	IDENTIFIER
Deposited Data		
Microarray	GEO	GSE21032
DNA methylation dataset	GEO	GSE73549
DNA methylation dataset	GEO	GSE38240
scRNA-seq	This paper	ArrayExpress: E-MTAB-9578
RNA-seq	This paper	ArrayExpress: E-MTAB-9624
Experimental Models: Cell Lines		
PC3	ATCC	Cat# CRL-1435; RRID: CVCL_0035
293T HEK	ATCC	Cat# CRL-11268; RRID: CVCL_1926
Mouse Embryonic Fibroblasts (MEFs)	This paper, see methods	N/A
Experimental Models: Organisms/Strains		
Mouse: <i>Pten</i> ^{pc/-}	Chen Z, et al. 2005	N/A
Mouse: <i>Pten</i> ^{pc/-} ; <i>Trp53</i> ^{pc/-}	Chen Z, et al. 2005	N/A
Mouse: <i>TIMP</i> ^{-/-} (TIMP1 B6.129S4-Timp1tm1Pds/J)	The Jackson Laboratory	Cat# 006243 RRID: IMSR_JAX:006243
Mouse: B6.SJL-Ptprc ^a Pepc ^b /BoyCrI (C57BL6-Ly5.1)	Charles River	N/A
Oligonucleotides		
See Table S3		
Recombinant DNA		
pMSCV-CRE-PURO-IRES-GFP	Addgene plasmid	Cat# 50935; RRID: Addgene_50935
pMSCVPURO-IRES-GFP	Addgene plasmid	Cat# 18751; RRID: Addgene_18751
GIPZ Sh-TIMP1 (107)	Horizon Discovery	Cat# RHS4430-200284994- V3LHS_317107
GIPZ Sh-TIMP1 (110)	Horizon Discovery	Cat# RHS4430-200284918- V3LHS_317110
pLX313-Firefly luciferase	Addgene plasmid	Cat# 118017; RRID: Addgene_118017
GIPZ Empty Vector	Horizon Discovery	Cat# RHS4351
pSicoR-Ef1a-mCh	Addgene plasmid	Cat# 31847; RRID: Addgene_31847
Software and Algorithms		
Image J	N/A	https://imagej.nih.gov/ij/ RRID: SCR_003070
Aperio ImageScope	Leica (V 12.3.2.8013)	https://www.leicabiosystems.com/digital-pathology/manage/aperio-imagescope/ RRID: SCR_014311
GraphPad Prism	GraphPad software (V 8.4.2 (679))	https://www.graphpad.com/scientific-software/prism/ RRID: SCR_002798
FlowJo	FlowJo LLC	https://www.flowjo.com/solutions/flowjo RRID: SCR_008520
Sequence data, analyses		
Cell Ranger (3.1.0)	10X Genomics	https://support.10xgenomics.com/single-cell-gene-expression/software/pipelines/latest/what-is-cell-ranger
R v4.0.2	https://www.r-project.org/	NA

(Continued on next page)

Continued

REAGENT or RESOURCE	SOURCE	IDENTIFIER
R package Seurat v3.2.0	https://satijalab.org/seurat/	RRID: SCR_016341
STAR v.2.5.1b	https://github.com/alexdobin/STAR	RRID: SCR_015899
Other		
jetPRIME®	Polyplus transfection	Cat# 114-07/712-60
Click-iT™ EdU Pacific Blue™ Flow Cytometry Assay Kit	Invitrogen	Cat# C10418

RESOURCE AVAILABILITY

Lead Contact

Further information and requests for resources and reagents should be directed to and will be fulfilled by the Lead Contact, Andrea Alimonti (andrea.alimonti@ior.usi.ch).

Materials Availability

Mouse lines generated in this study are maintained at IRB mouse house facility and are available upon request.

Data and Code Availability

The accession number for the scRNA seq reported in this paper is ArrayExpress: E-MTAB-9578. The accession number for the RNA-seq reported in this paper is ArrayExpress: E-MTAB-9624. The public datasets used are from GEO with the accession numbers: GSE21032, GSE73549, GSE38240.

EXPERIMENTAL MODEL AND SUBJECT DETAILS

Mouse Models

All mice were maintained under specific pathogen-free conditions in the animal facilities of the IRB institute, authorization number TI-2015062501. Experiments were performed according to the state guidelines and approved by the local ethical committee ("Dipartimento della Sanita' e Socialita', Esperimenti su animali," Canton Ticino), authorization number TI-04/2017 and TI-51/2018.

Prostate-specific *Pten*^{pc-/-} and *Pten*^{pc-/-}; *Trp53*^{pc-/-} transgenic mice (Chen et al., 2005) were crossed with *Timp1*^{-/-} mice (Jackson Laboratory, 6243) to generate *Timp1* knock out in *Pten*^{pc-/-} and *Pten*^{pc-/-}; *Trp53*^{pc-/-} prostatic epithelia. The experiments started at age of 9 weeks; only male mice were used. NSG male mice, at 8-9 weeks of age, were used for the development of the *in vivo* metastatic model upon intravenous injection of PC3 shCtrl and shTIMP1.

MEFs Production and Cell Culture

Primary Mouse Embryonic Fibroblasts (MEFs), were obtained from individual embryos of *Pten*^{loxP/loxP}, *Pten*^{loxP/loxP}; *Trp53*^{loxP/loxP} and *Pten*^{loxP/loxP}; *Timp1*^{-/-} genotype from a pregnant mouse at 13.5 days post-coitum. Embryos were harvested and the individual MEFs were cultured in DMEM containing 10% fetal bovine serum (FBS) and 1% Penicillin/Streptomycin (P/S).

Human Tissue Microarray (TMA)

Human TMA samples were processed and obtained from Universitätsspital Zürich (USZ) (Zhong et al., 2016). Three independent TMA samples were stained for PTEN and TIMP1 as follows: ZTMA76, ZTMA80, and ZTMA204. Human TMA samples from TAX2501 study as previously published (Antonarakis et al., 2012) was obtained and stained for TIMP1 antibody. PTEN status was correlated (Antonarakis et al., 2012) with TIMP1 staining quantification.

Prostate Cancer Cell Culture

PC3 human prostate cancer cells were purchased from ATCC and were cultured according to the manufacturer's instructions. Cells were cultured in RPMI 1640 supplemented with 10% FBS and 1% P/S. HEK-293T (human embryonic kidneys) cells were obtained from ATCC. Cells were cultured in DMEM supplemented with 10% FBS and 1% P/S. All cell lines were kept under controlled temperature (37°C) and CO2 (5%) and used for experiments at early passages. All the cell lines were tested negative for Mycoplasma (MycAlert™ mycoplasma detection kit, LT07-418, LONZA).

METHOD DETAILS

Transgenic Mouse Model Treatments

Pten^{pc-/-}; *Timp1*^{-/-} male mice were treated with Navitoclax (ABT263) (MedChem express, HY-10087), intraperitoneally at a dosage of 50mg/kg, daily for two weeks (Demaria et al., 2017), whereas *Pten*^{pc-/-} and *Pten*^{pc-/-}; *Timp1*^{-/-} male mice were treated with Docetaxel

(TEVA Pharma AG 6984894) intraperitoneally at 10mg/kg once a week for 6 weeks (Di Mitri et al., 2014; Toso et al., 2014). Mice were monitored for any suffering of distress or weight loss by measuring total body weight of mice weekly and monitoring the behavioral changes every day for a total of 4 weeks of treatment.

Transgenic Mouse Model Bone Marrow Reconstitution

Bone marrow reconstitution experiment was performed by flushing the femurs of male *Pten*^{pc+/+}; *Timp1*^{+/+} (CD45.1) mice under sterile conditions with RPMI 1640 using a 21-gauge needle. Recipient C57BL/6 *Pten*^{pc-/-}; *Timp1*^{-/-} CD45.2 male mice were lethally irradiated (900 cGy radiation) and transplanted intravenously with viable bone marrow cells from *Pten*^{pc+/+}; *Timp1*^{+/+} (CD45.1) mice. Peripheral blood was examined for immune-cells reconstitution by FACS stainings for CD45.1 and CD45.2. Lymph nodes were analysed for metastases by H&E and PanCK stainings after mice euthanasia.

Generation *In Vivo* Experimental Metastatic Model

The metastatic *in vivo* model was generated upon injection of a total of 200'000 PC3 shCtrl and shTIMP1 cells expressing luciferase plasmid (pLX313-Firefly luciferase) injected intravenously (I.V.) in NSG mice.

These mice were monitored to visualize the tumor cells and their spread to distal organs using IVIS imaging system (IVIS spectrum, Perkin Elmer) on weekly basis. Xenolight D-luciferin (Perkin Elmer, 122799) at 150mg/kg was injected in mice 12 mins prior IVIS spectrum imaging. Mice were treated with vehicle, Docetaxel (10mg/kg once a week for 6 weeks) and ABT263 (50mg/kg, daily for two weeks).

Upon completion of study, mice were euthanized by CO₂ asphyxiation, and tissues were procured for histological, mRNA and protein analyses.

Generation of *Pten* KO MEFs

To prepare lentiviral particles, HEK-293T cells were transfected using JetPRIME® transfection reagents (JetPRIME®, Polyplus transfection, 114-07/712-60) as the manufacturer's instructions. Primary MEFs were infected with retroviruses expressing either pMSCV-CRE-PURO-IRES-GFP or pMSCV-PURO-IRES-GFP for 48 h and selected with Puromycin at a concentration of 3µg/ml. MEFs were treated with Pan-MMPs inhibitor (Millipore, GM6001) at 10 µM and Docetaxel at 10 nM.

Generation of shTIMP1 Human Prostate Cancer Cell Line

PC3 cell line were transfected with shRNA using the following human TIMP1-directed shRNA a. RHS4430-200284994-V3LHS_317107 and b. RHS4430-200284918-V3LHS_317110. To prepare lentiviral particles, HEK-293T cells were transfected using JetPRIME® transfection reagents (JetPRIME®, Polyplus transfection, 114-07/712-60) as per the manufacturer's instructions. PC3 cells were infected with the filtered lentiviral supernatant obtained from transfected HEK-293T cells. Infected human prostate cancer cells were subsequently selected using Puromycin (3µg/ml).

ABT263 was used at the concentration of 2.5 µM, docetaxel was used at 5µM.

Immunohistochemistry (IHC) and Immunofluorescence (IF)

For both IHC and IF tissue sections were processed as follows: deparaffinized, unmasked, pre-staining, blockings and secondary stainings. Deparaffinization was performed using three-step procedure, first and second step the slides were immersed in OTTIX plus solution (Diapath, Cat No. X0076) for 5 mins each followed by third and last step of OTTIX shaper solution (Diapath, Cat No. X0096) for 5 mins. The slides were drained off the excess solution and were then immersed in ionized water for 5 mins. Further, unmasking or antigen retrieval procedure was followed which involved immersing the section slides in pH solutions (depending upon the antibodies) either pH 6 (Citrate, Company: Diapath, Cat No. T0050) or pH 9 (DAKO, Cat No. K800421-2) in water bath at 98°C for 20-25 mins. The slides were allowed to cool at room temperature for 20-25 mins. The section slides were washed with 1xPBST (0.5% Tween20), 2 times for 3 mins each, followed by staining procedure. Only for IHC but not for IF, blocking procedure began by incubating the slides with 3% H₂O₂ (VWR chemicals, Cat no: 23615.248) for 10 mins followed by 1xPBST washes as before and performing protein block. For both IHC and IF, protein blocking was performed using Protein-Block solution (DAKO Agilent technologies, Cat No. X0909) for 10 mins at room temperature. Depending upon antibodies, if they were developed in mouse host, the tissues were blocked for mouse cross-reactivity using biotinylated Anti-Mouse antibody (Vector Laboratories, Cat No. BP-9200). Sections were stained with respective primary antibodies at room temperature for 1 hour followed by 3 washes with 1xPBST as before. These slides were further incubated with respective secondary antibodies, for IHC, Anti-Mouse (Vector Laboratories, Cat No. BP-9200), Anti-Rabbit (Vector Laboratories, Cat No. BP-9100) and for IF using aluminum foil to protect from light, Fluor chrome antibodies (conjugated either with Alexa- 488, -594). In both cases, secondary antibodies were diluted at 1:200 in 1xPBS solution for 30 mins at room temperature. For IF, upon completion of secondary antibody incubation procedure, slides were washed 3 times with 1xPBST with minimum exposure to light and upon draining out the PBST, slides were incubated with mounting media with DAPI (Invitrogen, P36931) ready to be visualized under fluorescent confocal microscope. For IHC, during secondary antibody incubation, Vectastain ABC solution was prepared (Company: Vector laboratories, Cat No. PK-6100) at the dilution of 1:150 of both Solution A and Solution B in 1xPBS solution followed by 30 mins incubation at room temperature. Upon completion of secondary antibody stainings, slides were washed for 3 times with 1xPBST followed by ABC solution staining for 30 mins at room temperature. After ABC, slides were washed 3 times with 1xPBST and final steps of IHC stainings were performed. DAB staining was performed using DAB solution

(Company: Vector laboratories, Cat No. SK-4105. One drop of Chromogen in 1ml of Diluent solution) and allowed to stain for no more than 3–4 mins at room temperature. Immediately slides were washed 3 times with 1xPBST and counter staining was performed using hematoxylin solution (Diapath, C0303). At the end of IHC staining, sections were dehydrated using deparaffinization procedure after which slides were mounted with coverslip using aqueous mounting media (Diapath, 060200). Normal, tumor tissue and lymph node samples were fixed in 10% neutral-buffered formalin (Thermo Scientific, Cat No. 5701) overnight. Tissues were washed thoroughly under running tap water followed by processing using ethanol and embedded in paraffin according to standard protocols. Sections (5 μ m) were prepared for antibody detection and hematoxylin and eosin staining. Slides were prepared consecutive sections. For determination of metastases, lymph nodes, lungs and kidneys were longitudinally sectioned at 5 μ m through the entire tissues.

Senescence associated β -galactosidase (SA- β -gal) Assay

For tissue-specific SA- β -gal assay, tumor samples were immediately frozen in OCT solution at -80°C and sections of 4 μ m were prepared. Senescence-associated SA- β -gal staining was performed using Senescence β -Galactosidase Staining Kit (Cell Signaling Technology, Cat. No 9860) according to the manufacturer's instructions. Counter staining was performed using Eosin staining (Alcohol-based Diapath, C0352). For *in vitro* experiment, SA- β -gal staining was performed using the Senescence β -Galactosidase Staining Kit according to the manufacturer's instructions.

Single Molecule Fluorescent In-Situ Hybridization

Mice were sacrificed and the prostate tumors were fixed in 4% PFA (Santa Cruz Biotechnology, sc-281692) in 1x PBS for 3 hours and subsequently incubated in 30% sucrose, 4% PFA in PBS overnight at 4°C . Fixed tissues were embedded in Tissue-Tek OCT Compound (Sakura, 4583). 8 μ m thick sections were cryo-sectioned onto poly L-lysine coated coverslips and air-dried for 15 min before proceeding to hybridization according to a published smFISH protocol (Farack et al., 2019). Probe libraries were designed using the Stellaris FISH Probe Designer Software (Biosearch Technologies) and coupled to Cy5 (GE Healthcare, PA25001), Alexa594 (Thermo Fisher, A37572) as previously published (Itzkovitz et al., 2011; Lyubimova et al., 2013). DAPI (Sigma-Aldrich) was used as nuclear counterstain. Tissue sections were then treated with 1X TrueBlack Lipofuscin Autofluorescence Quencher (Biotium, 23007) to remove signal from auto-fluorescent granules. Slides were mounted using ProLong Gold (Molecular Probes, P36934). The smFISH imaging was performed on a Leica THUNDER 3D Live Cell Imaging system using the following THUNDER Computational Clearing Settings, Feature Scale (nm): 350, Strength (%): 98, Deconvolution settings: Auto and Optimization: High.

Single Cell Sequencing Analysis

Prostate tumors were resected from *Pten*^{pc/-} and *Pten*^{pc/-}; *Timp1*^{-/-} mice (all three lobes, AP, DLP and VP) and were processed for single cell suspension followed by RNA sequencing and analysis using the following procedure:

Single Cell Suspension

prostate tumors were isolated, minced and processed for single cell suspension. Tissues were digested in 2 ml of Digestion Buffer composed by RPMI 10% FBS + 1% P/S, 500 μ L of Collagenase D (1 mg/mL), 50 μ L of DNase (100 U/mL) and 125 μ L of HEPES (25 mM). The cell suspension was incubated for 1 hour at 37°C on a rocker. Then, the digestion was stopped adding 1 mL of RPMI 10% FBS + 1% P/S. The cells suspension was filtered through a 100 μ m cell strainer and kept on ice for 4 minutes. Then cells suspension was filtered again through a 40 μ m cell strainer and spun down at 1500 rpm for 5 min at 4°C . FACS staining was performed using the following antibodies: anti-Epcam-FITC and anti-CD45-APC and the cells were sorted in three different tubes: Epcam+, CD45+ and Epcam-/CD45-. After counting, cells were mixed together in ratio 1:1:1 to perform single cells sequencing.

Single-cell transcriptomes was performed using 10X Chromium single cell platform (10X Genomics, Pleasanton, CA, USA). FACS-sorted Epcam+, CD45+ and Epcam-/CD45- prostate cells were used in equal ratio as the input source for the scRNA-seq. Cells were suspended in a phosphate buffer solution containing 0.04% weight/volume bovine serum albumin (BSA). The recommended volume of single cell suspension was loaded on a Chromium Single Cell Controller (10x Genomics) targeting ~6000 cells per sample. Bar-coded single-cell gel beads in emulsion (GEMs) were created by 10x Genomics® Chromium TM and then reverse transcribed to generate single-cell RNA-seq libraries using Chromium Single Cell 3' Library and Gel Bead Kit v2 (10X Genomics) according to manufacturer's instructions. Resulting short fragment libraries were checked for quality and quantity using an Agilent 2100 Bioanalyzer and Invitrogen Qubit Fluorometer. Unique molecular identifiers (UMIs), which were incorporated into the 5' end of cDNA during reverse transcription, were used to quantify the exact number of transcripts in a cell.

Single-Cell Sequencing Analysis

Sequencing data were processed by CellRanger (version 3.1.0) and reads were aligned to mouse genome (mm10 v3.0.0) with STAR (v.2.5.1b). To reduce the 'dropout' phenomenon, RMagic package was used on gene-counts (van Dijk et al., 2018). Single cell sequencing analysis was performed in epithelial cells purified from both *Pten*^{pc/-} and *Pten*^{pc/-}; *Timp1*^{-/-} tumors. The samples of both mouse models were integrated using Seurat package (*IntegrateData function*). In the epithelial compartment (Epcam+ cells), we used *AddModuleScore function* to define senescence score (based on *p16*, *p21*, *p27*, *p19* and *Pai-1* genes expression). We performed hierarchical clustering, an algorithm that clusters similar data into groups (method = "complete" in *phetmap function*), and we divided the epithelium population into four main groups, Cluster_3 included cells with high senescence score. We also performed a correlation analysis using Pearson's correlation coefficient is the test statistics between *Bcl2* expression and the senescent scores.

Proliferation Assays

Proliferation assay in MEFs was performed by plating 10^4 cells per well of 24-well plate in triplicate while in PC3 cell lines was performed by plating $1-2 \times 10^4$ cells per well of 24-well plate in triplicate. For each time point, cells were washed twice with 1x PBS followed by 10 mins fixation using 10% Formalin (Thermo Fisher Scientific, 5701). After fixation, formalin was aspirated followed by 2 washes with 1x PBS and thereafter stained with crystal violet (Sigma, V5265) for 15 mins. Staining solution was washed using tap water and allowed to dry overnight. Representative images of the plates were obtained using an image scanner and the cells were destained using 10% acetic acid solution on the shaker at room temperature for 30-40 mins. The crystal violet dye extracted from the cells was measured using spectrophotometer at 590 nm.

Invasion and Migration Assay

For both invasion and migration assay 8.0 μm Boyden chambers were used (Falcon, 353097). For invasion assay the boyden chambers were covered with 100 μL of phenol-red-free matrigel mix (Corning, 356231) which was diluted 1:3 portions with DMEM for MEFs and RPMI for PC3 cells (FBS-free) with 5% BSA (VWR, 0332) filtered with 0.22 μm filters. Thereafter, these chambers were placed in a 24-well plate and were incubated for 30 mins at 37°C. For both invasion and migration assay 50'000 PC3 and 30'000 MEFs were plated under serum-starved condition in Boyden chambers. Chambers were placed in 24-well plate containing complete media with 10% FBS. This would allow the cells to acquire invasive and migratory phenotype. The experiment was stopped after 36-48 hours of incubation. Equal number of cells was seeded in wells underneath to normalize the invasion and migration assay to cell proliferation.

Co-culture Experiment

PC3-sh*TIMP1*-GFP cells were plated in 10 cm cell culture dish at 300'000 cells seeding density. These cells were treated with vehicle and Docetaxel (10 nM) for 2 days and subsequently with ABT263 (5 μM) alone and in Docetaxel-treated cells overnight. Then, PC3-sh*TIMP1*-GFP were washed and PC3 parental cells expressing mCherry plasmid (pSicoR-Ef1a-mCh) were added at 300'000 seeding density. Four days post co-culturing, cells were fixed and stained for EdU stainings (Invitrogen, C10418) according to the manufacturer's instructions and analyzed by FACS to determine the proliferative index in cells.

Condition Media and Protein Profiler Assay

Cells supernatants were harvested and spun down at 1500 rpm for 10 mins. For heat-inactivation, condition media were boiled at 95°C for 5 mins. Before to analyze the condition media on protein profiler assay, the supernatant was filtered using 0.22 μm filters and the protein concentration was measured using BCA kit (Thermo Fisher, 23227) according to manufacturer's instructions. Protein concentrations were measured using spectrophotometer at 562nm. For Timp1 detection, *Pten*^{pc-/-}, *Pten*^{pc-/-}; *Trp53*^{pc-/-} tumor and WT prostate samples were resected and processed for single cell suspension and sorted for epithelial cells using anti-EPCAM-FITC antibody (Toso et al., 2014). Protein profiler array used to identify substrates of MMPs released in the media: for mouse samples, ARY028 (R&D systems) whereas for human samples ARY022B (R&D systems) according to manufacturer's instructions. Analysis was performed using protein array analyzer (Image J).

Recombinant Experiment

MEFs and PC3 cells were incubated with recombinant proteins: rIGFBP2 (R&D systems, CF-674-B2-025, 100 ng/ml), rIGFBP3 (R&D systems, CF675-B3-025, 200 ng/ml), rIGFBP5 (R&D systems, 578-B5, 500 ng/ml), rGDF15 (Peprotech, 120-28C, 10 ng/ml), rFGF1 (Peprotech, 450-33A, 10 ng/ml), rTF (Novus, NBP2-52327, 10ng/ml), rPEDF (R&D systems, 8295-SF, 200 ng/ml). Along with these, neutralizing GDF15 antibody (Abgent, ALS11572, 2.5 $\mu\text{g/ml}$) and FGFR inhibitors were also used (Medchem express, HY-15599, 2.5 μM). Incubation was performed for 48 hours after which equal number of cells from all the respective conditions was seeded for migration assay.

Western Blot

Mouse prostates, tumor samples or cells were lysed using 1x RIPA buffer (Cell signaling, 9806) supplemented with Phenylmethane-sulfonyl fluoride (PMSF; Millipore Sigma, catalog 329-98-6) and incubated on ice for 20 mins. Samples were centrifuged at 14'000 rpm for 15 mins. Protein concentration was determined by the BCA kit (Thermo Fisher 23227). Equal amounts of protein were subjected to SDS-polyacrylamide gel electrophoresis (SDS-PAGE), 8 or 10 or 12 % based on the molecular weight of the proteins of interest and transferred on to 0.45 μm nitrocellulose membrane (Thermo Scientific, 88018). After protein transfer, membranes were blocked in 5% milk solution and membranes were probed with the indicated antibodies overnight at 4°C. The membranes were incubated with horseradish peroxidase-conjugated (HRP-linked) secondary antibodies anti-rabbit IgG (Promega, W4011, 1:5000) or anti-mouse IgG (Cell signaling, W4021, 1:5000) and developed using enhanced chemoluminescence (ECL) substrate (Thermo Scientific, 32106). Membranes were exposed to Fusion Solo S imaging system (Vilber). Blots were semi-quantitatively analyzed by densitometry using ImageJ 1.52 v (National Institutes of Health).

Antibodies

Primary and secondary antibodies were used at the concentrations indicated in the [Key Resources Table](#) according to manufacturer's instructions.

Gelatin-Zymography

Zymography assay was performed by running 50 μ g of protein samples with the loading dye (Bio-Rad, 161-0764) 2 times the volume of the protein sample on gelatin-gel. Resolving gel: 30% acrylamide 0.8% bis-acrylamide (Bio-Rad, 1610156), 1.5M Tris HCl, pH 8.8, ddH₂O, Gelatin solution (Gelatin powder (Sigma, G1890) 100mg in 4.5ml of H₂O and 0.5ml of 10% SDS, 10% Ammonium Persulfate solution and TEMED. Stacking gel: 30% acrylamide 0.8% bisacrylamide (Bio-Rad, 1610156), 0.5M Tris HCl, pH 6.8, ddH₂O, 10% Ammonium Persulfate solution and TEMED. Samples were run at a constant voltage of 90 V. Gel was incubated with 1x Renaturation buffer (Bio-Rad, 161-0765, 10x) for 30 mins followed by 30 mins of 1x Developmental buffer (Bio-Rad, 161-0766, 10x). A subsequent processing was performed using 1x Developmental buffer for additional 60 mins followed by gentle shaking of gel in Buffer 3 overnight at 37°C. Buffer 3 (For 250 mL): In 235 mL of water, add 2.5 mL of Triton-X, 12.5 mL of 1 M Tris-HCl (pH 7.5, for 50 mM), 625 μ L of 2 M CaCl₂ (for 5 mM final) and 2.5 mL of 0.1 M ZnCl₂ (for 1 μ M final). After overnight incubation, gels were stained with Coomassie Brilliant Blue R-250 (Bio-Rad, 161-0436) followed by a destaining solution (methanol 400 mL, Acetic acid 100 mL in 500 mL water). Bands were acquired using Fusion Solo S (Vilber).

PCR Genotyping

Small (1-2 mm²) mouse ears biopsies were used for genotyping. For MEFs genotyping, we isolated genomic DNA from embryonic tails and limbs. Primers for genotyping are listed in Table S3. The PCR reaction was performed using PCR BIO Rapid Extract PCR Kit (PB10.24).

Quantitative Real-Time PCR (qRT-PCR)

RNA extraction from cells or tissues samples was performed using Trizol (Ambion, life technologies, 15596026), according to the manufacturer's instructions. cDNA was obtained using ImPROM II kit (Promega, A3800) according to the manufacturer's instructions. qRT-PCR was performed using KAPA SYBR FAST ABI qPCR Master Mix solution (KAPA Biosystem) on Step One Real-Time PCR systems (Applied Biosystems). Primers used for qRT-PCR are listed in Table S3. Expression levels were calculated using the $\Delta\Delta$ CT method (Livak and Schmittgen, 2001).

Gene Expression Profiling

RNA sequencing was performed at the Institute of Oncology Research using the NEBNext Ultra Directional II RNA library preparation kit for Illumina and sequenced on the Illumina NextSeq500 with single-end, 75 base pair long reads. The overall quality of sequencing reads was evaluated using a variety of tools, namely FastQC, RSeQC (Wang et al., 2012), AfterQC (Chen et al., 2017) and Qualimap (Garcia-Alcalde et al., 2012). Sequence alignments to the reference mouse genome (GRCm38) was performed using STAR (v.2.5.2a) (Dobin et al., 2013). Gene-expression was quantified at gene level by using the comprehensive annotations made available by Gencode (Harrow et al., 2012). Specifically, we used v20 release of the Gene Transfer File (GTF). Raw-counts were further processed in the R Statistical environment and downstream differential expression analysis was performed using the DESeq2 pipeline (Love et al., 2014).

Genes characterized by low mean normalized counts were filtered out by the Independent Filtering feature embedded in DESeq2 ($\alpha = 0.05$). Gene-set enrichment testing/analysis was performed using Camera (Wu and Smyth, 2012). Statistical enrichments were determined for gene-sets obtained from the Hallmark collection, which is curated by the Molecular Signature DataBase (MSigDB) (Liberzon et al., 2015; Liberzon et al., 2011).

RNA sequencing analysis was performed in two tumor regions (TA1 and TA2) from a total of 39 prostate tumor samples obtained from men with localized PCa who were scheduled for radical prostatectomy from a cohort of 1,200 patients within the ProCOC study (Umbehr et al., 2008). RNA sequencing was performed at the Functional Genomics Center Zurich. Briefly, from 39 prostate cancer patients, RNA was isolated from normal tissue, and TA1 and TA2 wherein these areas of tumors were chosen with highest tumor grade. A total of 39 normal, 39 TA1 and 27 TA2 RNA samples were obtained. RNAseq reads were aligned to genome using STAR aligner and the expression of genes was calculated using "featureCounts" program. Furthermore, these reads were normalized using "voom" program. RNA sequencing data was submitted to the Sequencing Read Archive (SRA) at NCBI under accession number PRJNA579899.

TCGA and GEO DNA Methylation Analysis

GEO datasets were downloaded from Gene Expression Omnibus (<http://www.ncbi.nlm.nih.gov/geo/>), including GSE73549 (a sum of 92 samples) and GSE38240 (12 samples). TCGA DNA methylation dataset, which included 479 primary prostate cancer patients, were collected from TCGA project (<http://cancergenome.nih.gov/>). Illumina HumanMethylation450K beadchips were used to detect the methylation levels for all of the above datasets. Beta value of selected CpG sites were used as the measurement of methylation.

Five CpG sites (cg04791822; cg04791822; cg18009325; cg27151711; cg16523424) located in the promoter region of the *TIMP1* gene were studied in all datasets. We retrieved gene-expression and DNA-methylation from The Cancer Genome Atlas (TCGA). Methylation level of *TIMP1* was determined as the mean of β -values within ± 1000 bp distance from the transcription start site (TSS). Samples were classified into quartiles based on methylation levels of *TIMP1*. Chi-squared test was used to determine the dependency between expression and methylation of *TIMP1*, between *TIMP1* expression and PTEN deletions/mutations and between *TIMP1* expression and PTEN expression. P-values were adjusted for multiple comparison analysis using Benjamini & Hochberg procedure (Benjamini and Hochberg, 1995). The statistical analysis and graphs were performed using R version 3.6.0 (<https://www.r-project.org>).

RNA-Seq Dataset Analysis

The RNA-Seq dataset was obtained from the TCGA database, which includes 479 primary prostate cancer patients. The within-lane normalization method to adjust for GC-content effect was used on the raw read counts and it was regarded as the measurement for gene expression quantification. We assessed the significance of the differential gene expression by comparing the TIMP1 high versus low methylated group of patients (mentioned above) by a negative binomial generalized log-linear model using the TCGAbiolink package in R-bioconductor (Colaprico et al., 2016). For identification of differentially expressed genes, p-value less than 0.05 was set as the criteria for statistical significance.

QUANTIFICATION AND STATISTICAL ANALYSIS

All experiments were performed on biological replicates as mentioned in the respective figure legends. Sample size for each experimental group/condition is reported in the appropriate figure legends. All data points are presented for quantitative data, with an overlay of the mean with SEM. Statistically significant differences between control and experimental groups were determined using Multiple Student's t-tests (two-tailed, unpaired), one-way ANOVA with Tukey multiple comparison difference test, Wilcoxon test, and log-rank (Mantel-Cox) test as indicated in the appropriate figure legend and text. All statistical analyses were performed using GraphPad Prism 8, Microsoft Excel 2016 or R-Studio.